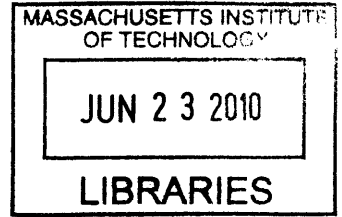# Molecular Dynamics Modeling of Ionic Liquids in Electrospray Propulsion

by

Nanako Takahashi

M.Eng., Aeronautics and Astronautics, Kyushu University, 2007

B.Eng., Mechanical and Aerospace Engineering, Kyushu University, 2005

Submitted to the Department of Aeronautics and Astronautics
in partial fulfillment of the requirements for the degree of

Master of Science in Aeronautics and Astronautics

at the

MASSACHUSETTS INSTITUTE OF TECHNOLOGY

June 2010

Author . . . .
Department of Aeronautics and Astronautics
May 18, 2010

Certified by . . . .
Prof. Paulo C. Lozano
H. N. Slater Assistant Professor
Thesis Supervisor

Accepted by . . . .
Prof. Eytan H. Modiano
Associate Professor of Aeronautics and Astronautics
Chair, Committee on Graduate Students

Molecular Dynamics Modeling of Ionic Liquids in Electrospray Propulsion

by

Nanako Takahashi

M.Eng., Aeronautics and Astronautics, Kyushu University, 2007

B.Eng., Mechanical and Aerospace Engineering, Kyushu University, 2005

Submitted to the Department of Aeronautics and Astronautics
on May 18, 2010, in partial fulfillment of the
requirements for the degree of
Master of Science in Aeronautics and Astronautics

Abstract

Micro-propulsion has been studied for many years due to its applications in small-to-medium sized spacecraft for precise satellite attitude control. Electrospray thrusters are promising thrusters built upon the state of the art in micro-technology and with flexible performance in terms of their high efficiency and high specific impulse. One challenge is to investigate in detail the mechanism for ion emission to complement experimental results and understand better how emission occurs in the micro to nano scale. Thus, atomistic modeling is used to understand properties of emitted charged particles which determine how the thrusters perform.

As a preliminary study of ion emission from Taylor cones, ion evaporation from 3 - 5 nm droplets was observed in molecular dynamics (MD) simulations to validate the atomistic modeling and to investigate activation energies. Ion emission was examined in terms of internal and external electric fields and the activation energies of each case were obtained using Schottky's model and direct energy calculation to compare with experimental values. Ion emission was mainly observed with electric field strengths between 1.2 -2.0 V/nm and the emitted species include both solvated and non-solvated ions. Propulsive properties from Taylor cones are examined using results from the analysis of electric current from ion emission.

In addition to an observation of ion emission from liquid droplets, numerical simulations for interactions between a solid plate and liquid droplets were conducted with MD simulation. It was concluded that another selection of force field needs to be considered to pursue further details, such as electrochemical effects.

Thesis Supervisor: Prof. Paulo C. Lozano
Title: H. N. Slater Assistant Professor

Acknowledgments

With the deepest gratitude, I would like to thank my best ever advisor Professor Paulo Lozano for all the support and for giving me an amazing opportunity to work on this interesting research at MIT. He always encourages me to move forward my research and to enjoy my life.

I would like to thank Professor Markus Buehler for opening the first gate for me to get into Molecular Dynamics world. His class was obviously the best one I have ever taken and his guidance for my research was always brilliant.

I would like to acknowledge Professor Manuel Martínez-Sánchez and Dr. Oleg Batishchev for having me in SPL and for fruitful discussions.

My funding sources allowed me to keep concentrate on research. I would like to express gratitude to the financial support from US Air force, Department of Defence and Japanese government ministry of education, culture, sports, science and technology.

I would also like to acknowledge all of my friends in SPL, Bobby, Anthony, Steve, Taylor, Murat, BJ, Mike, Taki, Tim, Carmen, Maria, Pablo, Carla, Ryan and particularly Dan. Anthony greatly helped me and guided me in a whole new culture when I first came to MIT and was having a lot of trouble with the English language. Dan supported me in every way from academic issues to lost in translation issues. He generously listened to what I am saying in poor English and always gave me brilliant advice. Also he kindly came to exotic Japan.

To my precious friends for their support and love: members of "Shitennou" Sho Sato and Yusuke Kobayashi and everybody in the Japanese Association of MIT, especially Masahiro "Hiro" Ono. Thank you for the brightest days. My talented chamber music trio member, Joey Zhou and Drew Wolpert, playing classical music with them has always healed my heart for past three years. My life has never been wonderful without "new grad social" members. Thank you for everything, Elza, Beenie, Leo, Bjorn, Britt, Cam, Jerome, Ulric, Alice, Zakiya, Sunny and Caley. You are so awesome! I never forget how fun it was when we were hanging out together.

Ghassan, the best ever TA, taught me the basics of Molecular Dynamics and how to enjoy MIT classes. My UROP, Michael Lieu, thank you so much for every effort you made to help me.

I would like to appreciate my boyfriend Shinji Tanaka for his eternal loving support during my most stressed period ever. I will also keep supporting you forever.

Finally, I would like to thank my family, Dad, Mom, Kun and my grandmas who support me from across the ocean.

Unfortunately I could not achieve my "original" goal, but I never stop exploring nature and world.

Fluctuat nec mergitur.

Contents

List of Figures

12

List of Tables

Chapter 1

Introduction

1.1 Electrosprays

Electrospray is a technology to produce ions/droplets from conductive liquids using a relatively simple setup as shown in Figure 1-1. Ion/droplet emission occurs at the apex of a liquid cone which is generated when a high electric potential between an extractor and conductive liquid is applied. There are several types of emitters with the most common being the capillary-type often used in mass spectrometry. The other types are externally wetted emitters (Figure 1-2) and porous emitters. For any kind of emitter, there are two underlining requirements: to locally enhance electric fields at the tip so that a liquid cone appears and to transport the liquid from a resevoir to the emission site. The cone is called a Tayor cone in honor of G.I. Taylor who first derived a mathematical model for ideal conditions in 1964 [1]. Details of the emission mechanism and Taylor cones will be discussed in section 3.1 and 3.2.

As for the applications of elecrosprays, they can be used in a broad field of studies from biology to space technologies. Mass spectrometry for biological molecules is the most well know application of electrosprays and was subject of the Nobel prize winning work by J.Fenn in 2002 [2], Some other technologies are: thin-film deposition and painting [3], electrospining which is used to create uniform strands of nano-scale fibers [4], micro scale atomizers for fuel injection [5],[6], molecular imaging applications [7], and focused ion beams (FIB) [8],[9],[10].
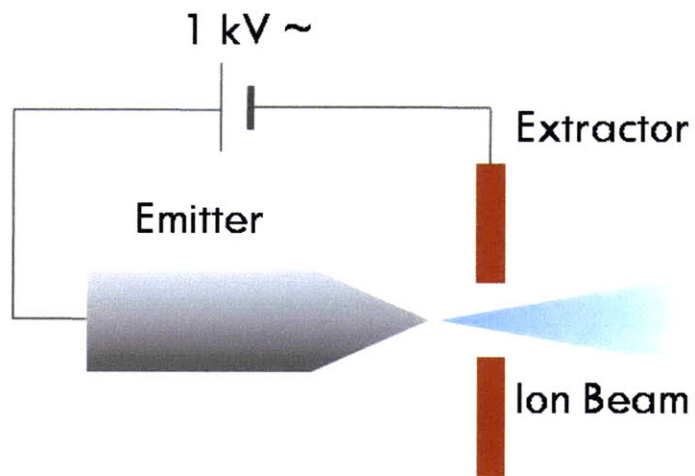
Figure 1-1: Schematic of electrospray setup
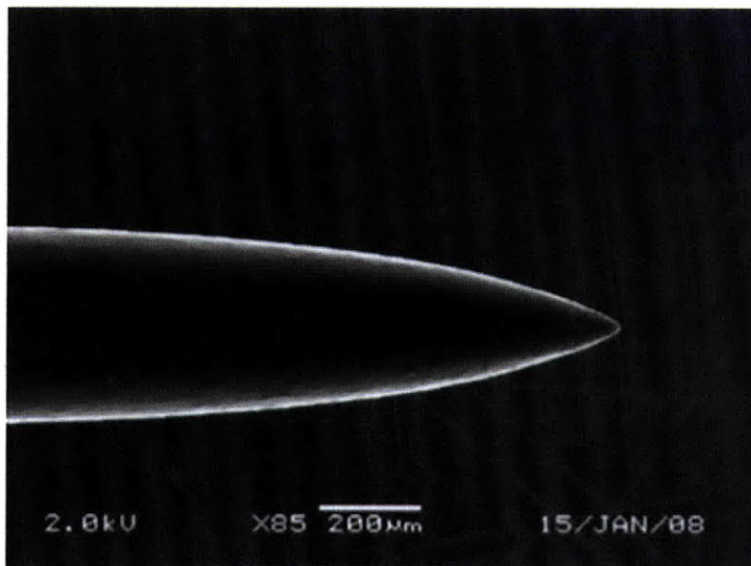
Figure 1-2: Tip of externally wetted electrospray thruster. Courtesy of A. Zorzos (MIT)

An application for space propulsion is explained in chapter 2.

1.2 Electrospray History

The use of electric fields for controlling fluids can be traced to the eighteenth and nineteenth century. [11],[12] The breakup of a charged liquid drop, Coulomb fission, was predicted by Rayleigh in his analytical work in 1882. [13] He presented that the instability occurs when the forces of electrostatic repulsion of surface charges exceed the forces of surface tension for a droplet. Zeleny first conducted an experiment of the observation of the Rayleigh instability and visual formation of cone-jet structures with a diluted solution of hydrochloric acid in 1914. [14],[15] However, the research was hidden from space propulsion applications for a half century until Krohn's electrospray research in 1961. [16],[17]

Unfortunately electrosprays were not pursued further as a thruster in the 1960's because the value of mass to charge ratio (m/q) was too large which requires high accelerating voltages (10 to 100kV) from $V = \frac{mc^2}{2q}$, even though higher particle mass is an attractive feature because it can effectively increase the thrust density. [18] In the same period, the theoretical model of cone formation was developed by Taylor (see detail in section 3.2). [19] Since then, electrospray research did not see significant progress until the breakthrough achieved by Fenn in the late 1980's, escalating an interest in nanotechnology. Fenn's contribution made it possible to utilize electrospray technology in mass spectrometry, while at the same time enabling a reduction of the mass to charge ratio. Fenn was awarded the Nobel Prize in Chemistry in 2002. [20] With this achievement and growing interest in ionic liquids, electrospray propulsion research embarked on a new era. Ionic liquids are molten salts at room temperature containing anion and cations exclusively, which allow a purely ionic regime of emission during electrospray use for extraction voltages under 2kV. [21],[22],[23]

As for studies of ion evaporation from a droplet, Thomson and Iribarne derived the threshold electric field at which ion field evaporation occurs before Coulomb fission. Emission is triggered by adding the energy to overcome the barrier associated

with both the solvation energy of the evaporated ion and the electrostatic interaction between the ion and the droplet with the assumption that the barrier is approximately 4-5 $\mathring{A}$ from the droplet surface [24]. In addition, they showed that the critical electric field is approximately 1 V/nm for droplets less than 10 nm in diameter using a kinetic model and charge mobility experiments in the late 1970's. [25] The Loscertales and Fernández de la Mora group and the Fenn group concluded the critical value for the evaporation of singly charged ions was between 0.7 and 1.9 V/nm. [26]

The detailed mechanisms of field evaporation are still not well understood because the complex particle-particle interactions of the thermalized droplets.

Chapter 2

Electrosprays in Space Propulsion

2.1 Electric Propulsion

Space propulsion systems, and rockets in general, provide force to accelerate space-craft consuming propellant. [27] The propulsion systems are used both for launch of spaceship from the Earth and for moving spacecraft in space. For instance, space thrusters are used for orbital maneuvers, north-south station keeping (NSSK), orbital altitude and attitude maintenance and interplanetary travel for deep space exploration. There are mainly two types of the systems: chemical and electric (Figure.2-1).

Chemical propulsion thrusters work by the conversion of an enthalpy increase from the energy of chemical reactions into jet kinetic energy of reaction producs (combustion), while electric propulsion makes use of electric energy to produce thrust.

Chemical

Electrical → Augmented

→ **Electrostatic** → **Electrospray**

→ Hall Thruster

→ Ion Thruster

→ Electromagnetic

→ Radio Frequency
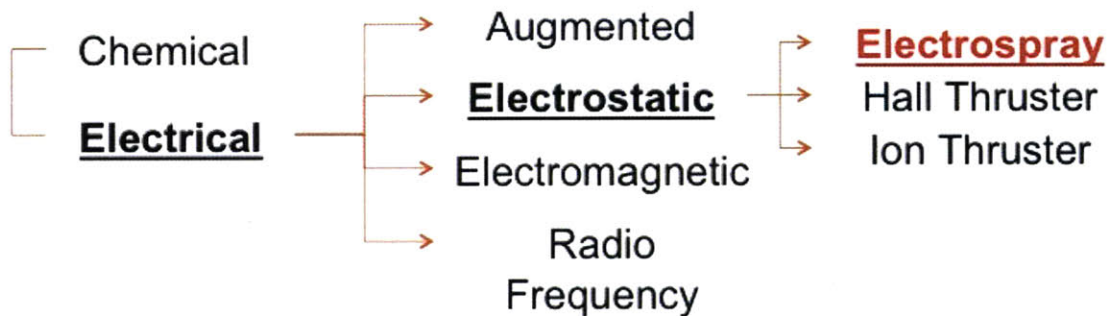
Figure 2-1: In-space propulsion technology

Electric propulsion also needs propellant to accelerate and since thrust depends on the electric power available, the thrust of electric propulsion is typically smaller than chemical propulsion. Electric propulsion is used in space, a vacuum environment, due to the low densities required by most electric discharges. [28]

There are several ways to transfer electric power to the propellant: electrothermal, electrostatic, and electromagnetic devices.

Electrothermal thrusters include the Resisto-jet and arc-jet which are augmentated devices which are primarily chemical thrusters but use electrical power to improve their performance. The propellant gas is heated electrically and expanted through a nozzle to convert its thermal energy to a jet of directed kinetic energy. Electrospray thrusters are electrostatic devices as well as ion thrusters in which the electrostatic forces accelerate ions/droplets. [29] Working details of electrospray thrusters are explained in section 2.1.1. For electromagnetic thrusters, the acceleration of a body of ionized gas is obtained by the interaction of currents driven through the gas with magnetic fields established either by the currents or by external means.

2.1.1 Electrostatic Thrusters

Typical electrostatic thrusters are ion thrusters and electrospray thrusters. In these devices, the electrostatic forces that accelerate the ions/droplets are also directly applied to electrodes, and this is how the structure receives thrust. Ion thrusters extract ions from ionized propellant by a potential drop through grids while electrons are emitted from a cathode which is placed at the exit of the thruster. These electrons neutralize the ion beams, avoiding spacecraft charging. Ion thrusters typically have specific impulses in the 3000 to 4000 range with power efficiencies as high as 75 percent. One of restrictions in ion thrusters is space charge limitation which is a phenomena in which the amount of extracted ions are limited due to their shield effect to the applied fields. On the other hand, electrosprays are not largely affected by space charge limitation because the emitter to extractor spacings are significantly smaller in electrospray devices. In addition, electrospray thrusters do not suffer from problems

associated to gaseous propellants. One of the main issues in electrospray thrusters is the transportation of liquid propellant from a reservoir to the emitter needle tips. In recent work, micro-fabricated porous emitters have been studied as they provide sufficient hydraulic impedance to sustain emission even at low currents. [30],[31]

2.2 Electrospray Thruster Application

In a broad sense, field emission electric propulsion (FEEP) and colloidal engines have identical principle of operation with our electrospray thrusters. The main differences are: (a) FEEP uses a liquid metal which requires high operation voltages (>5kV) due to its high surface tension and produce only positive beams.[32] Colloidal engines can be used with organic liquids with relatively high conductivity and lower surface tension which allows lower voltages (1kV). (b) Electrospray and FEEP thruster focus on ion emission to obtain high efficiency although colloidal engines could be nearly as efficient operating with droplets. In short, electrospray thruster families in general can adapt to missions through several regimes and types of liquids. Droplet regime gives low Isp/current due to its large specific charge, on the other hand, ion regime gives high Isp/current though the mixed regime decrease thrust performance. [33] These flexibility of characteristics within electrospray thrusters give options to many kind of space missions.

The following is a list of potential applications for electrospray thrusters:

1. Precise attitude control of spacecraft

   The small thrust allows accurate positioning of spacecraft. One example is the LISA Pathfinder mission which features both FEEP and colloidal thrusters and plans to be launch in 2013. [34] The colloidal thruster was developed by Busek Company in the U.S.. One of advantages of electrospray thrusters is that they do not need conditioning time which is usually required for other electric propulsion and FEEP thrusters. Liquid metal used for FEEP propellant needs to be heated up to liquefy.

2. Main propulsion for Nano/Micro satellites

With growing demand of miniaturization of spacecraft components and satellites themselves, electrospray thrusters have the potential of providing main propulsion to small satellites. CubeSats are one example of small satellites, which are widely considered in universities and companies because of their advantages in small satellite space science and exploration at lower costs. CubeSats and other nano satellites have typically a volume of 1 liter and weight no more than 1 kg. Most thruster technologies are larger than the satellite itself. Also, the fuel is fed by capillarity action in electrospray thrusters therefore avoiding a complex fuel feed system which takes space in satellites. Another option might be micro-scale cold gas thrusters [35], however it has a problem to miniaturize the thruster without downgrade the performance and the Isp is limited. FEEP and colloid thrusters have a possibility to contaminate a spacecraft and specific impulse of colloid thrusters is generally lower than electrospray thruster.

Chapter 3

Electrospray Physics

3.1 Surface charge

The basic physics of electrospray can be expressed by balance between surface traction by external electric field and surface tension of liquids. The external electric field can be related with the electric field in the liquid using Gauss' Law [29], and for dielectric liquid,

$$E_{n,liquid} = \frac{1}{\epsilon} E_{n,gas} \tag{3.1}$$
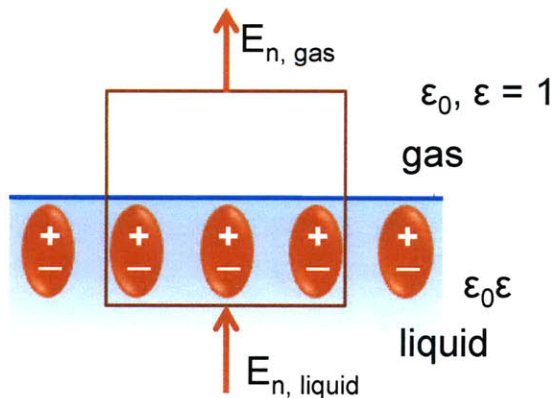
Figure 3-1: Schematic of surface charge for dielectric liquid

Here, ϵ is dielectric constant of liquid. This can take large values and for perfect

conductors, the field inside liquid becomes zero which is caused by high mobility free electrons with fast relaxation times.

Thus, the relaxation time can be considered as another important aspect of electrosprays. The liquid takes time to respond to external electric fields and this depends on the mobility of charged particles.

Conductivity is expressed using mobility of positive and negative particle:

$$\kappa = ne(\mu^+ + \mu^-) \tag{3.2}$$

The rate of free surface charge density (σ_f) accumulation is,

$$\frac{d\sigma_f}{dt} = \kappa E_{n,liquid} \tag{3.3}$$

where the surface charge density can be obtained by Gauss' law:

$$\sigma_f = \epsilon_0 E_{n,gas} - \epsilon\epsilon_0 E_{n,liquid} \tag{3.4}$$

From equation 3.3 and 3.4,

$$\frac{d\sigma_f}{dt} + \frac{\kappa}{\epsilon\epsilon_0}\sigma_f = \frac{\kappa}{\epsilon}E_n^g \tag{3.5}$$

Solving the differential equation,

$$\sigma_f = \frac{E_{n,gas}}{\epsilon_0}\left(1 - e^{-\frac{t}{\tau}}\right) \tag{3.6}$$

where $\tau = \frac{\epsilon\epsilon_0}{\kappa}$ is the relaxation time, or the time to reach equilibrium in the charge distribution.

3.2 Taylor cone

Taylor cones are produced when conductive liquids are placed under an external electric field. [29],[19] Taylor estimated the shape assuming that the cone formed by a balance between electric pressure and surface tension. This is expressed by:

26
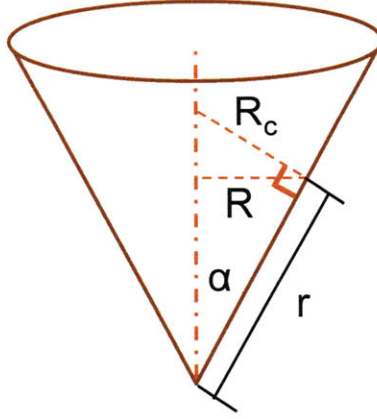
Figure 3-2: Taylor Cone Schematic

$$\frac{1}{2}\epsilon_0 E_{n,liquid}^2 = \frac{\gamma}{R_c} \tag{3.7}$$

Here, γ and $1/R_c$ represent surface tension and curvature which is shown in figure 3-2. Using geometric relations, the right hand side of equation 3.7 is

$$\frac{\gamma}{R_c} = \frac{\gamma}{R}cos\alpha = \frac{\gamma}{r}cot\alpha \tag{3.8}$$

From both equations 3.7 and 3.8, the electric field along the surface of the liquid cone is obtained:

$$E_{n,liquid} = \sqrt{\frac{2\gamma cot\alpha}{\epsilon_0 r}} \tag{3.9}$$

The schematic of electric field along liquid cone surface is shown in figure 3-3. From equation 3.9, it is obvious that electric field is proportional to $r^{-1/2}$ therefore it is smaller upstream and at the tip of cone the electric field becomes infinite. Large electric fields induce ion emission. However, it is challenging to numerically analyze the tip region due to its small dimension and dramatic potential gradients, thus alternate models are used, such as the sphere on cone (SOC) model. The detailed calculation is shown in section 7.3.

Following his calculation, Taylor mathematically derived that the inner half-angle is independent of liquid properties and has a universal value of 49.3°. Real experi-
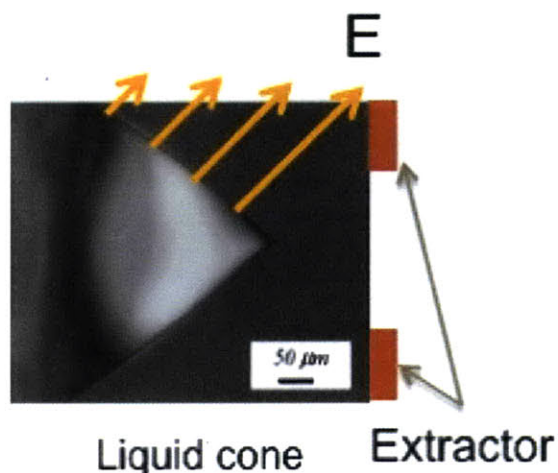
Figure 3-3: Schematic of liquid cone and electric of liquid surface

mental cones show a remarkable resemblance to Taylor cones, even though the apex singularity in real cones is removed by the emission of a charged liquid jet in most solvents [36] or the emission of ions in ionic liquids and metals.

3.3 Activation energy

Ion emission can be explained using arguments from statistical mechanics and defining the energy needed for ion evaporation, or activation energy. Iribarne and Thomson first presented a model to describe ion evaporation from charged droplets. [24]

Here we derive the fundamental equation, Schottky's equation, using the equilibrium between ions in the liquid and gas phases. [37] In equilibrium, ions evaporate from the liquid surface into the gas phase and also the opposite happens. Equilibrium can be expressed as:

$$(\mu_i)_{l,s} = (\mu_i)_{g,v} \tag{3.10}$$

where μ, i, l, s, g, v correspond to chemical potential, ion, liquid, surface, gas and volume.

Assuming Maxwell-Boltzmann gas, the above equation would be,

$$kT_l \ln \left(\frac{Q_{l,s}}{N_{l,s}} \right) = kT_g \ln \left(\frac{Q_{g,v}}{N_{g,v}} \right) \tag{3.11}$$

where k is Boltzmann constant and T is temperature, which in equilibrium, $T_g = T_l$. Q and N represent the partition function and number of molecules, respectively.

Considering dimensional aspects which Q and N have (e.g. 2D for liquid surface and 3D for gas phase), the equation 3.11 is,

$$\frac{\frac{1}{A} Q_{l,s}}{\frac{1}{A} N_{l,s}} = \frac{\frac{1}{V} Q_{g,v}}{\frac{1}{V} N_{g,v}} \tag{3.12}$$

$$\frac{q_{l,s}}{n_{l,s}} = \frac{q_{g,v}}{n_{g,v}} \tag{3.13}$$

Here, A is area of the liquid surface and V is volume of the gas. Thus, q and n are the partition function and number of molecules per unit area and volume, respectively.

If we assume that the distribution function in gas is isotropic, the ion flux everywhere in gas can be derived as,

$$\Gamma \sim \frac{n_{g,v} \bar{c}}{4} \tag{3.14}$$

Here, $\bar{c}$ is the thermal velocity for a Maxwell distribution,

$$\bar{c} = \sqrt{\frac{8kT}{\pi m_i}} \tag{3.15}$$

where m_i is mass of ion.

Therefore the ion flux of equation 3.14 is,

$$\Gamma = n_{g,v} \sqrt{\frac{kT}{2\pi m_i}} \tag{3.16}$$

At the same time, from equation 3.13,

$$n_{g,v} \;=\; n_{s,l} \frac{q_{g,v}}{q_{l,s}} \tag{3.17}$$

$$=\; \frac{\sigma}{e} \frac{q_{g,v}}{q_{l,s}} \tag{3.18}$$

where σ is surface charge of the liquid surface and e is unit charge.

The partition function of the liquid surface is,

$$q_{l,s} \;=\; \frac{Q_{l,s}}{A} \tag{3.19}$$

$$=\; \sum_i \frac{e^{-\frac{1}{kT}\epsilon_i}}{A} \tag{3.20}$$

$$=\; \frac{1}{A} e^{-\frac{1}{kT}\left(\epsilon^{int} + \epsilon^{trans}\right)} \tag{3.21}$$

$$=\; \frac{1}{A} e^{-\frac{1}{kT}\epsilon^{int}} e^{-\frac{1}{kT}\epsilon^{trans}} \tag{3.22}$$

$$=\; Q^{int} q_{l,s}^{trans} \tag{3.23}$$

$$=\; Q^{int}\left(\frac{2\pi m_i kT}{h^2}\right) \tag{3.24}$$

where Q_l^{int} is the internal partition function of ions in the liquid phase which may include rotational, vibrational and excitational degrees of freedom and $q_{l,s}^{trans}$ is translational partition function of the surface per unit area. h is Planck's constant.

The partition function of gas can be obtained in the same way, but note that the energy reference is assumed at the liquid surface,

30

$$q_{g,v} = \sum_i \frac{e^{-\frac{1}{kT}(\epsilon_i + \epsilon_{ref})}}{A} \tag{3.25}$$

$$= Q^{int} q_{g,v}^{trans} e^{-\frac{\triangle G_0}{kT}} \tag{3.26}$$

$$= Q^{int} \left(\frac{2\pi m_i kT}{h^2}\right)^{3/2} e^{-\frac{\triangle G_0}{kT}} \tag{3.27}$$

where we define the energy reference difference between liquid and gas as $\triangle G_0$ which is called the free enthalpy or the activation energy, at the same time, this is the energy barrier to cross over the border between liquid and gas state. [38] Here the system is under equilibrium with constant pressure, temperature and number of molecules overall and this indicates that the free energies do not change.

Therefore together with equation 3.16, 3.18, 3.24 and 3.27, the current density becomes,

$$j = \sigma \frac{kT}{h} e^{-\frac{\triangle G_0}{kT}} \tag{3.28}$$

This current density can also be considered as the flow from the liquid surface. We can apply this argument to the liquid surface under electric field assuming that the liquid surface is not affected much by gas phase especially with the field. [24] In this case, the image charge model 3-4 which is similar theory to Schottky model of electron emission is applied.

Taking the x axis as in figure 3-4 and applying an electric field along it, the work required (potential energy) to move an extracted ion of charge e from x to infinity is, assuming that the binding force arises from its image charge,

$$W = \int_x^\infty F dx \tag{3.29}$$

Assuming the dielectric constant of material is low enough, the force on the charge by its image is,

31
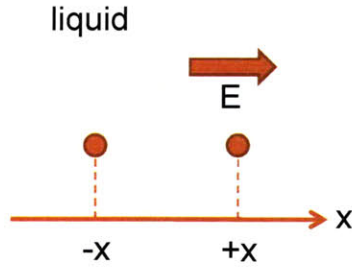
Figure 3-4: Schematic of image charge model.

$$F = \frac{-e^2}{4\pi\epsilon_0(2x)^2} + eE \tag{3.30}$$

Here we can see that the image charge pulls back the ion against the electric field. The equation 3.29 becomes,

$$W = \frac{-e^2}{16\pi\epsilon_0 x} - eEx \tag{3.31}$$

This energy is maximum when

$$x_{max} = \left(\frac{e}{16\pi\epsilon_0 E}\right)^{1/2} \tag{3.32}$$

and

$$W_{max} = -\left(\frac{e^3 E}{4\pi\epsilon_0}\right)^{1/2} \tag{3.33}$$

This is called the Schottky depression which reduces the energy barrier by the effect of charge and field. Thus, the equation 3.28 can be modified as,

$$j = \sigma\frac{kT}{h}\exp\left[-\frac{1}{kT}\left(\triangle G_0 - \sqrt{\frac{e^3 E}{4\pi\epsilon_0}}\right)\right] \tag{3.34}$$

To overcome the energy barrier $\triangle G_0$ solely by the electric field, the Schottky depression needs to be roughly equal to $\triangle G_0$. Therefore the electric field necessary is:

$$E \simeq \frac{4\pi\epsilon_0 \triangle G^2}{e^3} \qquad (3.35)$$

This indicates that the field evaporation occurs at around 1 - 2 V/nm [26] which corresponds to $\triangle G_0$ of 1.2 - 1.7 eV.

Chapter 4

Ionic Liquids

4.1 General Properties

Ionic liquids, also called room temperature molten salts (RTMS), are matter solely composed by ions, anions and cations, and their volatility is significantly lower than other liquids. [39],[40] This property is desirable for electrospray thrusters under vacuum conditions. The volatility of ionic liquids is low because the interaction between ions are dominated by Coulomb-type forces. It is possible to evaporate ions from an ionic liquid when an electric field of enough strength is applied perpendicular to the liquid surface which is shown in chapter 3. The volatility limit of ionic liquids has been recently probed spectroscopically [41] and by distillation [39]. The general conclusion is that the vapor pressure of ionic liquids, at moderate temperatures, remains negligible. Another attractive point is their high conductivity which enables a surface reaction to strong electric fields. In addition, they are not flammable and do rarely react with other materials, thus avoiding contamination of spacecraft systems in vacuum. However, some ionic liquids are sensitive to moisture and can be contaminated when exposed to atmosphere and also care is needed due to potential toxicity. The general characteristics of organic ionic liquids are shown in table 4.1. [42]

Ionic liquids have found applicability in many areas such as: green chemistry industry for their stable and organic nature, gas handling using ionic liquids as solvents

Table 4.1: Typical Characteristic of Organic Ionic Liquids

Low melting point	Treated as liquid at ambient temperature
	Wide usable temperature range
Non-volatility	Thermal stability
	Nonflammability
Composed by ions	High ion density
	High ion conductivity
Organic ions	Various kinds of salts
	Designable
	Unlimited combination

for wide variety of compounds and gases [43], nuclear industry for recovery of uranium and other metals from spent nuclear fuel and other sources [44], solar energy for use as a heat transfer and storage medium [45] and batteries [46]. More recently, magnetic ionic liquids have also been reported. [47]

4.2 EMI-BF$_4$

1-ethyl-3-methylimidazolium tetrafluoroborate (EMI-BF$_4$) is one of dialkyl-imidazolium cation family of ionic liquid. The general properties are shown in table 4.2.

EMI-BF$_4$ has one pair of large anion and small cation as shown in figure 4-1. The off-balance of size (e.g. large cation) has been considered as the reason why the liquid state is the most stable in ionic liquids. Another distinguishing property of EMI-BF$_4$ includes a strong tendency to supercool. [48] The electrical conductivity increases and the kinematic viscosity decreases with increasing temperature, same as typical organic fluids. [49] Another interesting characteristic has been identified: a

Table 4.2: EMI-BF$_4$ general properties

Melting point	[deg C]	12.0 - 12.5
Conductivity at room temp.	[Si/m]	1.3
Dynamic viscosity at room temp.	[Pa . s]	0.043
Density at room temp.	[kg/m^3]	1517
Surface tension at room temp.	[dyn/cm]	41
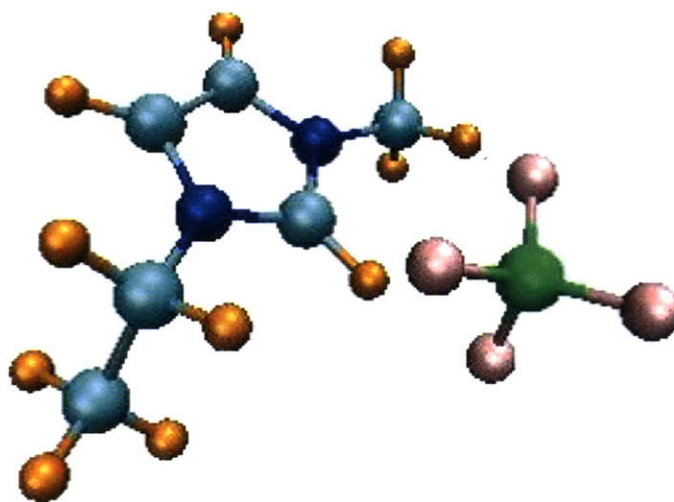
Figure 4-1: EMI-BF$_4$

phase-change in the vicinity of 333 K. [50] This is investigated by measuring diffusion coefficients and suggests the transformation of the diffusion particle from "discrete ion-pair" to "individual ion" at temperatures above 335K due to decomposition of the EMI-BF$_4$ ion pair.

Figure 4-2 shows partial charges of EMI-BF$_4$ according to de Andrade et al. [51]. The signs on atoms follows AMBER atom type. AMBER is a type of force field which is widely used for organic materials. The electric charge distribution of the ions by atomic point charges was calculated by quantum mechanics (QM) calculations on the ab initio level.

As for application to electrosprays, from the previous work[52], it is shown that EMI-BF$_4$ is one of the most widely used liquids in electrospray thruster research. Thrust efficiency with EMI-BF$_4$ is estimated to be higher compared to other kinds of ionic liquids in the work although efficiency is greatly affected by fragmentation of solvated ions. The detail of solvated ion is explained in next section.
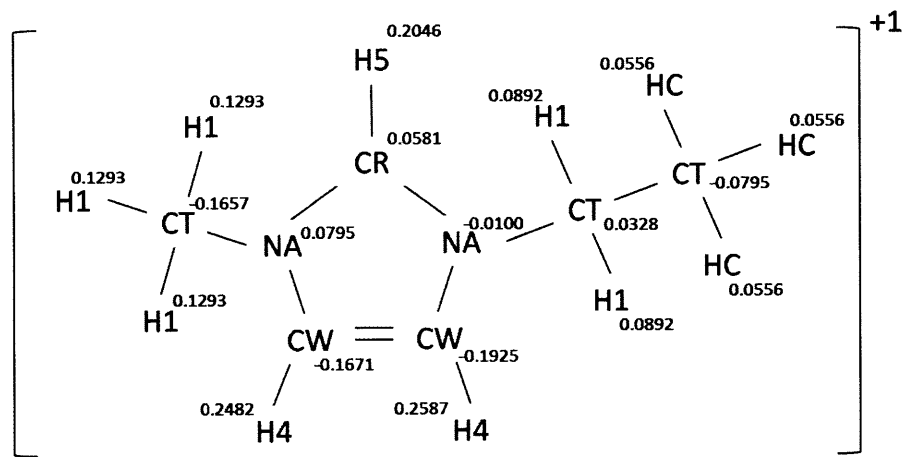
(a) EMI$^+$
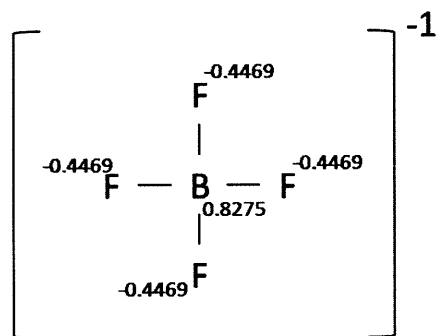
(b) BF$_4$

Figure 4-2: (a),(b) Chemical structural formulae with atom types and partial charges of EMI$^+$ anion and BF4$^-$ cation.

4.3 Solvated Ions

Solvated ions are defined here as ions attached to neutral pairs. For example, EMI-BF_4 can have $(EMI-BF_4)_n$ EMI^+ for a positive solvated ion and $(EMI-BF_4)_n$ BF_4^- for a negative solvated ion. n is defined as the number of solvation which is the number of neutrals attached to the ion.

In general, the solvation is caused by different types of intermolecular interactions: hydrogen bonding, ion-dipole and dipole-dipole attractions or van der Waals forces. [53] Ionic liquids are composed by polar molecules, thus, any of the above may happen to make solvated ions. In EMI-BF_4 or in other types of ionic liquid, solvated ions have been observed in time-of-flight (TOF) experiments. [52],[54],[55],[56],[57] Specifically, it is found by mass spectrometry that the species population peaks at $n = 0$ and $n = 1$, with significantly lower traces of ions with $n \geq 2$. Even though experimental observations are crucial in obtaining information on the macroscopic outcome of the field evaporation process, direct measuring techniques are unable to probe the emission mechanics at the molecular level. In addition to this, it is difficult to study the stability of solvated ions through experiments alone.

The simulation results regarding ion emission of solvated ions will be presented in chapter 7.

Chapter 5

Numerical Simulation Methods

Continuous formulations [58] an scaling analyses have been able to describe in detail the fluid dynamics of electrojets and the parametric relevance of ion emission. However, these approaches lose their ability to track the physics when the dimensions of interest become similar in size to the liquid molecules. Molecular dynamics (MD) is a powerful tool for investigating atomic-scale phenomena which takes into account intra- and inter- molecular forces. This enables us to segmentalize most materials into an atomistic scale at which continuum methods, like CFD, are not appropriate.

In this chapter, the basics of MD will be explained.

5.1 Molecular Dynamics Fundamentals

Molecular dynamics simulations have become a standard tool for the investigation of atomistic problem such as biomolecules or structural failure [59]. It basically contains four steps as shown in figure 5-1.

MD basically calculates the equation of motion to obtain coordinates and velocities of next step. Forces in the equation of motion are derived by differential calculus of potentials ($F_i = -\frac{\partial U(r_i)}{\partial r_i}$) which requires assumptions depending on conditions.
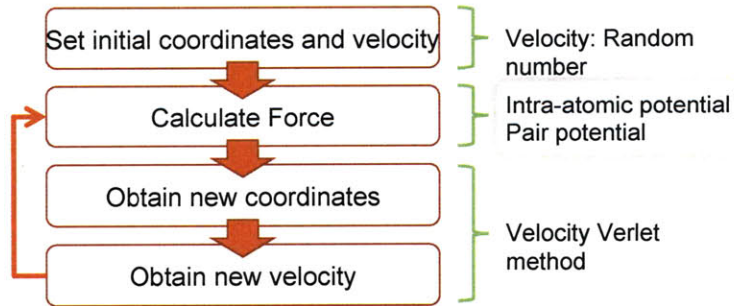
Figure 5-1: Molecular Dynamics fundamental procedure
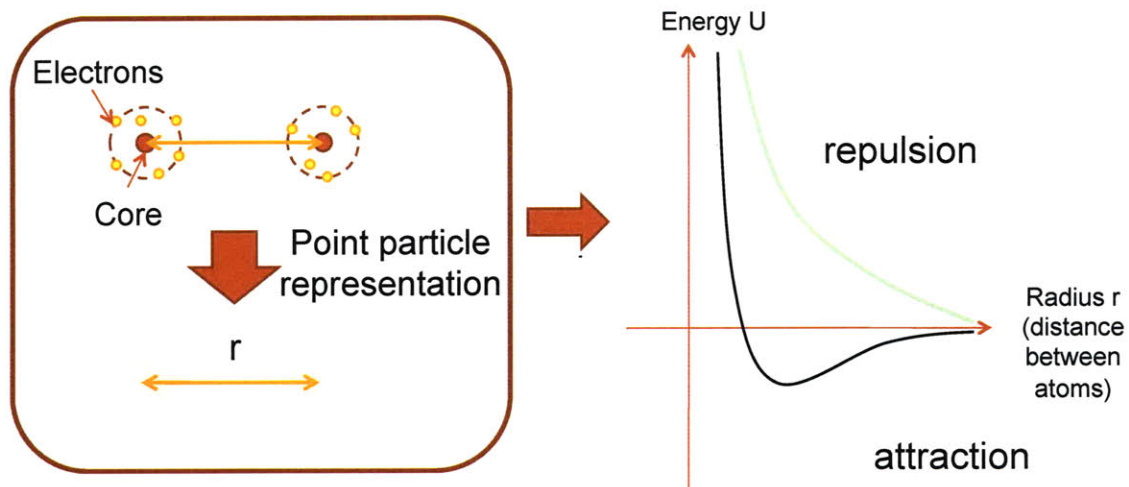
Figure 5-2: Schematic of point particle representation of covalent bond

5.1.1 Potentials in MD Simulations

MD does not directly calculate electrons and core interaction. They are represented as point particles and the interaction between point particles includes repulsion and attraction (figure 5-2). The black line in right graph of figure 5-2 is the sum of energies of repulsion and attraction forces and particle dynamics follow the energy profile. The repulsion and attraction are due to Pauli's exclusion and formation of chemical bond by sharing of electrons, respectively.

Here, we assume the EMI-BF$_4$ system has two types of potentials; intra-atomic potential and pair potential.
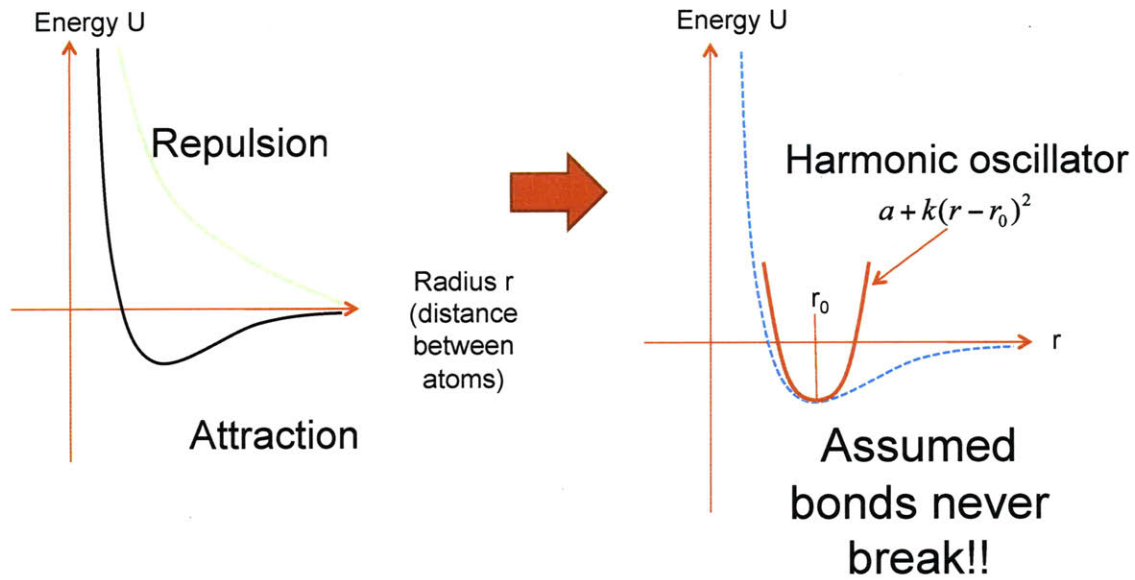
Figure 5-3: Molecular Dynamics fundamental procedure

The harmonic potential (figure 5-3) is applied to the intra-atomic potentials because it can be considered that atom bonds never break. As for the pair potential, we use electrostatic (Coulomb) potential and Lenard-Jones (van der Waals) potential [60].

The equation of the potentials is expressed as follow:

$$V_{\text{total}} = \sum_{\text{bonds}} K_r (r - r_{eq})^2 + \sum_{\text{angles}} K_\theta (\theta - \theta_{eq})^2$$
$$+ \sum_{\text{dihedrals}} \frac{K_n}{2} [1 + \cos(n\phi - \gamma)] + \sum_{i<j} \left[\frac{A_{ij}}{R_{ij}^{12}} - \frac{B_{ij}}{R_{ij}^6} + \frac{q_i q_j}{\epsilon_0 R_{ij}} \right] \quad (5.1)$$

where

$$A_{ij} = 4\epsilon_{ij} \sigma_{ij}^{12}$$

$$B_{ij} = 4\epsilon_{ij} \sigma_{ij}^{6}$$

Here, ϵ_{ij} is the traditional well-depth and σ_{ij} is the size parameter. K is the energy coefficient for each kind. r is a distance between atoms which are attached

43
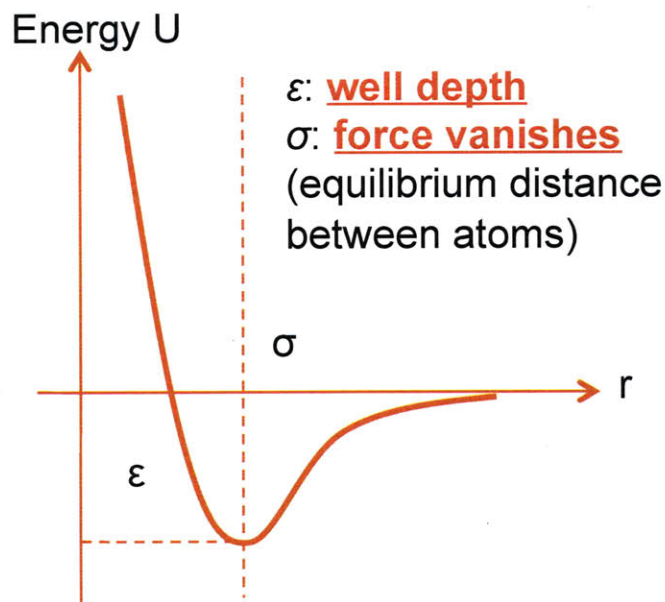
Figure 5-4: Schematic of Lennard-Jones (LJ) potential

each other by covalent bonds. θ is an angle within three atoms connected by covalent bonds. n and γ are coefficients for dihedral (torsional) angles which is formed on two planes. The plane is defined by three atoms connected by covalent bonds. ϕ is a dihedral angle. R is the distance between pair atoms. ϵ_0 is the permittivity of vacuum. q is a charge on atom. As for suffixes, they correspond to an equilibrium state. This typical AMBER force field expression and the first three terms represent covalent interactions: bond stretching, bending and torsion, respectively. The last term provides pair potentials for atom-atom interactions including Lenard-Jones (LJ) [60] and Coulomb terms.

The Lennard-Jones potential is the empirical model for van der Waals forces which are attractive or repulsion forces between nonbonded atoms. It is the fourth term of equation 5.1. The schematic of the potential is shown in figure 5-4. The well depth ϵ and σ corresponds to those in A_{ij} and B_{ij} in equation 5.1.
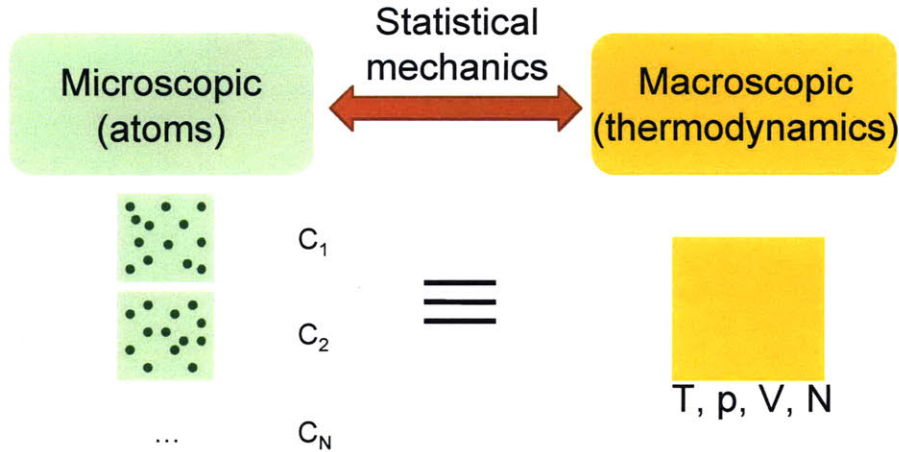
Figure 5-5: Thermodynamic ensemble schematic

5.1.2 Thermodynamic Ensembles

Another important aspect of MD are the thermodynamic ensembles which provide a robust framework to calculate a range of "macroscale" properties. MD provides snapshots of phenomena which are defined by extensive variables, which are proportional to volume and mass. However the macroscopic world is presented by intensive properties such as temperature and pressure. Macroscopic conditions translate to the microscopic system as boundary conditions. The distribution of microscopic states is related to the macroscopic conditions.

Effective method in MD derive from so-called Ergodic hypothesis, which suggests that ensemble (statistical) averages are equal to time averages and all microstates are sampled with appropriate probability density over long time scales.

$$\frac{1}{N_A} \sum_{i=1...N_A} A(i) = \langle A \rangle_{Ens} = \langle A \rangle_{Time} = \frac{1}{N_t} \sum_{i...N_t} A(i) \tag{5.2}$$

In a way, this is a point in common between Monte Carlo (MC) simulations and MD simulations. MC and MD can be compared in three ways.

1. How to obtain ensemble average

   MC: obtains ensemble average by random stepping scheme.

   MD: obtains ensemble average by dynamical solution of equation (time history).

45

2. Assumption

MC: Acceptance/rejection algorithm leads to proper distribution of microscopic states.

MD: Time average equals ensemble average (Ergodic hypothesis)

3. Dynamical information

MC: No dynamical information about system behavior (only equilibrium processes) - no "real" time

MD: Existence of dynamical information about system

5.1.3 Definition of Temperature

We assume the classical mechanics (kinetic theory) definition of temperature:

$$\frac{1}{2}m\langle c_i^2 \rangle = \frac{1}{N_f} \sum_{i=1...N_f} \left(\frac{1}{2}m\vec{v}_i^2 \right) = \frac{1}{2}k_B T \qquad (5.3)$$

where, N_f is the total number of degrees of freedom ($N_f = 3N$, N=Number of particles) and k_b and T are Boltzman constant and temperature in Kelvin, respectively. Here average kinetic energy per degree of freedom is related to temperature via Boltzmann's constant.

5.1.4 Time Step Selection

The idea is to keep time step as large as possible due to computational efficiency but not too large to cause error. The rule of thumb is that time step must be much smaller (100 ... 1000 times) than the fastest time-scale dynamics in the system, e.g. high frequency oscillations of light atoms (e.g. C-H bonds, O-H bonds). Typical vibrational frequencies is $\omega_0 = 10^{13}[sec^{-1}]$, thus it is common to select a time step of $10^{-15}sec = 1fs$. This was also the limit of time steps we found, and stable results could not be provided for time steps larger than 1 fs.

Chapter 6

Basic Numerical Simulation Procedure

This chapter explains three steps carried out in this research to apply an external electric field to an EMI-BF$_4$ droplet.

6.1 Modeling a Single Ionic Liquid Molecule

A three-dimensional system has been used in this computational model to ensure the mechanical integrity of the molecule. The optimized atom coordinates (Table 6.1) for a single EMI-BF$_4$ molecule were obtained by the semiempirical orbital program MOPAC 6 [61]. We verify that the cartesian set of coordinates corresponds to the structure of EMI-BF$_4$ indicated by Katsyuba et al [62]. The structure includes location of anion relative to cation. We use a force field which was introduced for EMI-BF$_4$ by de Andrade et al. [51]. The force field parameters are based on the AMBER force field [63], which contains a complete force field for liquid state EMI-BF$_4$ based on the results from both Quantum Mechanical (QM) and Molecular Mechanical (MM) simulations. Figure 4-2 shows the chemical structural formulae which indicate atom types and partial charges of EMI-BF$_4$, as they appear in the results of de Andrade et al.

Table 6.1: Single EMI-BF$_4$ coordinates. Unit in Å

Atom type	x	y	z
N	-1.543	0.630	-0.795
C	-0.169	-0.630	-0.795
N	0.270	1.934	-0.795
C	-0.853	2.780	-0.803
C	-1.988	1.964	-0.807
C	-2.370	-0.556	-0.690
C	-2.694	-1.214	-2.019
C	1.644	2.336	-0.684
H	-3.047	2.227	-0.805
H	0.492	-0.288	-0.737
H	-0.765	3.868	-0.798
H	1.693	3.363	-0.235
H	2.116	2.346	-1.703
H	2.188	1.604	-0.015
H	-1.815	-1.288	-0.020
H	-3.324	-0.250	-0.173
H	-1.767	-1.554	-2.540
H	-3.330	-2.110	-1.811
H	-3.255	-0.526	-2.695
B	1.233	-1.338	1.219
F	1.465	-1.697	-0.075
F	-0.114	-1.329	1.392
F	1.834	-2.182	2.072
F	1.691	-0.068	1.366

6.2   Equilibration of a Single Droplet

As the initial condition, 64 and 125 EMI-BF$_4$ molecules are aligned in cubic with potentials described in section5.1.1 (6-1). Each molecule has the coordinate obtained in previous section 6.1

Five different equilibrium states of 125 molecules are prepared at temperature intervals of 50 K between 250 K and 450 K for applied electric field simulations. Additional simulations at 300, 323 and 373 K are used in non-applied electric field cases. In a typical simulation, atoms in the droplet are allowed to interact until equilibrium is reached using a sequence of NVE and NVT ensembles. NVE ensemble
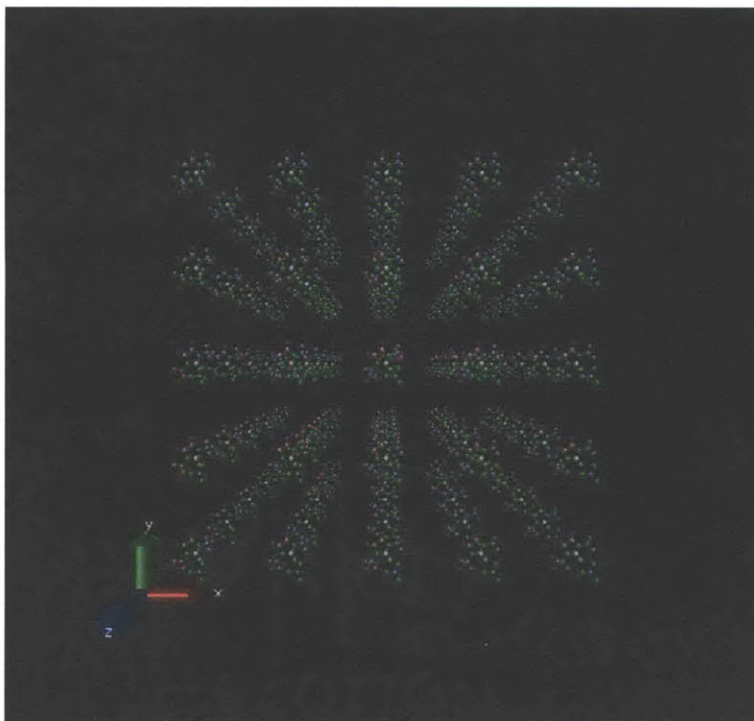
Figure 6-1: First stage of equilibration

is also called the microcanonical ensemble in which the number of moles, volume and energy are kept constant. In a similar way, NVT ensemble is called the canonical ensemble in which the number of moles, volume and temperature are kept constant.

Excess energy stored in the initial random coordinate distribution is released in an NVE ensemble. The procedure has several steps. In the first step the system is initialized at 10 K. As the simulation progresses, the temperature increases until converging to a higher value, in some instances near 700K. In the second step, the excess energy is released by initializing the coordinates with the set obtained at the end of the first step and adjusting the temperature back to 10 K. This procedure is repeated until the temperature converges to the target temperatures at every 50 K between 250 K and 450 K. The optimization of the structure is then performed with constant number of moles, volume, and temperature (NVT, canonical ensemble) using a Nosé-Hoover thermostat [64] with a temperature fluctuation of 100 K at the target initial temperature. These simulations are carried out with a cutoff distance of 200 nm for both the Lennard-Jones and the Coulombic potentials thus accounting

49

for every atom in the droplet. The equilibrium states of the EMI-BF$_4$ droplet of three different temperatures are shown in figure 6-2. The droplet has an ellipsoidal shape at least below 300 K because of the unsymmetrical shape of the ions.

The condition of an EMI-BF$_4$ droplet for 125 molecules after the equilibration is temperature: 300K, droplet diameter: 4 [nm] and EMI-BF$_4$ mass: 111[u] for EMI and 87 [u] for BF$_4$. From here, the computed density is 1.226 [g/cm^3], which can be compared against the comparing the experimental value of 1.24 [g/cm^3] at 295 [K] [65],[66].
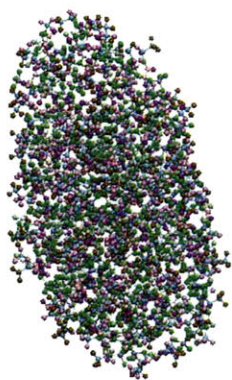
(a) 300K
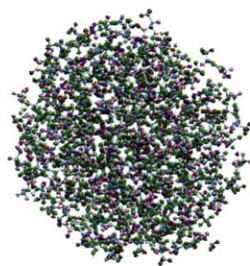
(b) 350K
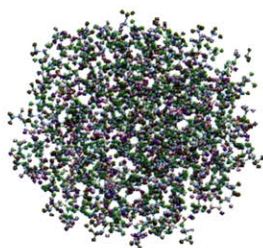
(c) 400K

Figure 6-2: Equilibrium state of EMI-BF$_4$ (a) 300K (b) 350K (c) 400K

6.3   Droplet Response to Electric Fields

Table 6.2: Simulation variations.

	E field types	E field [V/nm]	Temperature [K]	♮ of samples
Droplet	External	1.0-2.0	250-450	5
	Internal	-	300, 323, 373	3
Droplet + Tungsten	External	3.0-6.0	300	1

The electric field is applied once the equilibrium state is obtained for the different initial coordinates and temperatures (Table 6.2). The electric field is applied in two different ways: an external constant and homogeneous field and through adding or removing charges from the droplet. Here the second way is more realistic because electric fields are far from uniform in ion emiting from Taylor cones. Details of the droplet systems are explained in chapter 7 and 8 and the droplet and tungsten system is shown in chapter 9. The external constant electric field is applied in the x direction. In the molecular dynamics simulation, the additional force term ($\vec{F} = q\vec{E}$) is added to the fundamental equation 5.1 to include applied electric fields.

Examples of ion emission for positive and negative sides are shown in figure 6-3 and 6-4. Due to electric field in the x direction, positive ions are emitted to the right and negative ions is to the left. Once ions are emitted, the droplet is charged so it starts moving along the electric field. Although the NVE ensemble is used for the simulations, the energy from the electric field is added to the system at every time step. Thus, the droplet does not cool down even when in motion.

(a) 0 ps

(b) 51 ps

(c) 131 ps

(d) 152 ps
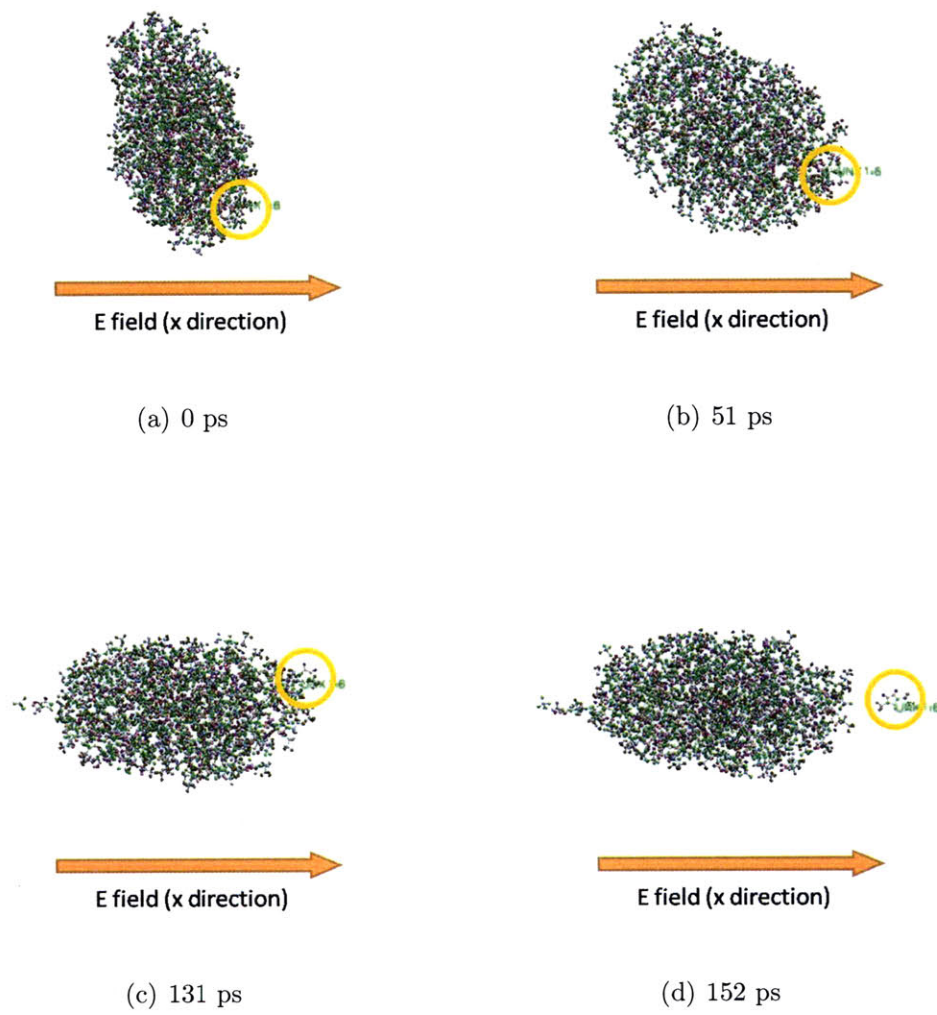
Figure 6-3: First ion emission in positive side
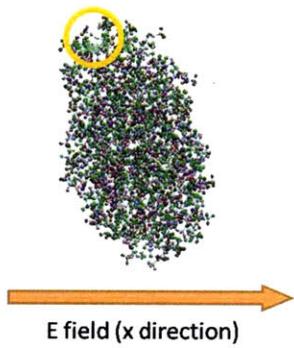
(a) 0 ps
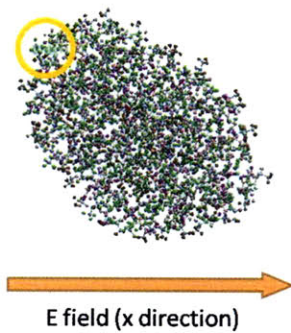
(b) 46 ps
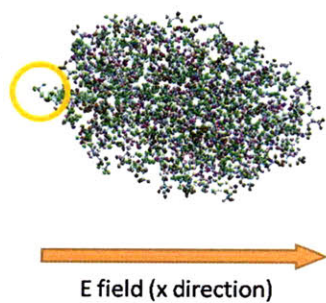
(c) 86ps
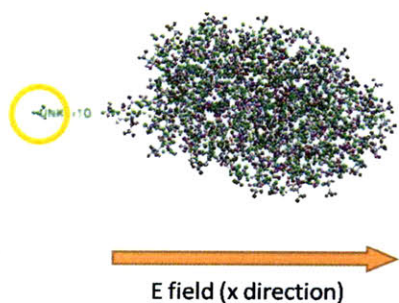
(d) 106 ps

Figure 6-4: First ion emission in negative side

Chapter 7

Ion Evaporation under Applied Electric Fields

7.1 Analysis of Electrical Currents

Once the electric field is applied, the droplet is polarized in the direction of the field (rotating in some cases due to the induced dipole of the highly unsymmetrical droplet (figure 7-1)) and eventually experiencing evaporation of non-solvated and solvated ions.

The emitted ions are observed at the edge of droplet along the direction of the electric field and currents are obtained from the ion dynamics. The current is estimated by counting the number of ions for both non-solvated and solvated ions that cross the liquid surface in a given time interval. The total number of positive and negative emitted ions for each electric field is approximately 60. Afterwards, the droplet collapses and retains nothing of the original form. Statistics of the emitted ions are obtained until the droplet itself starts to break up chaotically and observation of ion emission is difficult. Ion emission is observed mainly in the electric fields for 1.2 V/nm through 2.0 V/nm. The current profile as a function of applied electric fields are examined in this electric field range and is shown in figure 7-3 [76]. In the
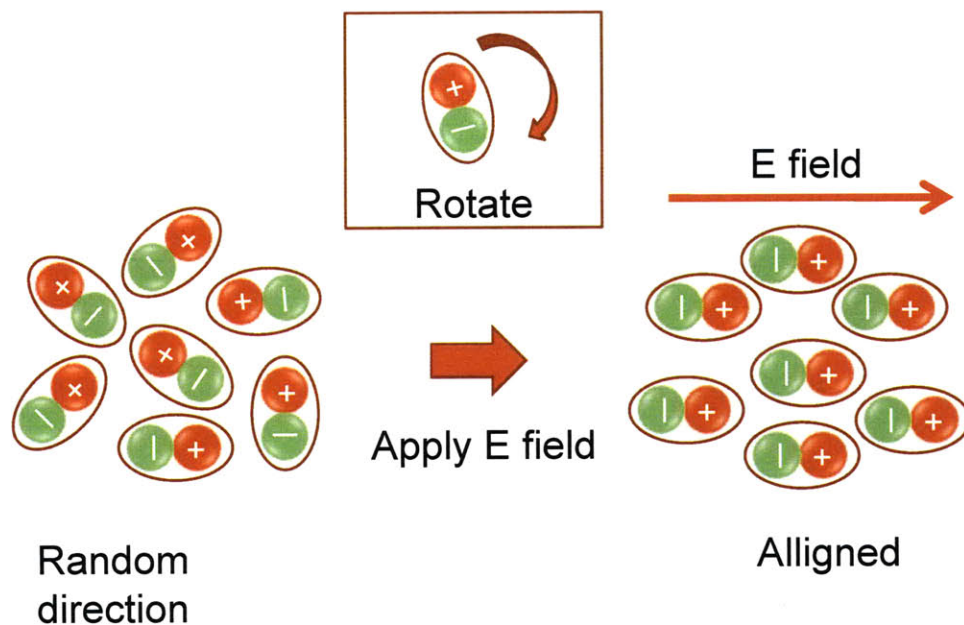
Figure 7-1: Schematic of droplet rotation

figure, the total current includes both solvated and non-solvated ions. Error bars indicate standard deviation of five samples. The total current profile is dominated by non-solvated ions in both positive and negative cases and the fraction of solvated ions is larger at smaller applied E fields. The maximum number of solvation is $n = 4$ in the positive side and $n = 5$ in the negative side.

We also examined current profiles as a function of temperature to estimate the activation energy of ion evaporation using Schottky's model [24]. The detail of the activation energy analysis is discussed in section 7.4.1. The current profile is specifically measured at an applied electric field of 1.4 V/nm (figure 7-3). As expected, the current increases with temperature and the total current is dominated by non-solvated ions.
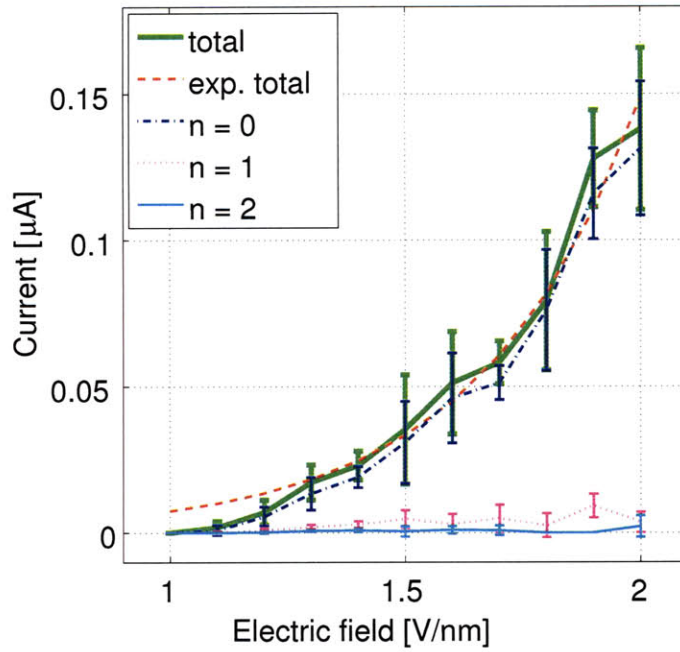
(a) $(EMI\text{-}BF_4)_n EMI^+$
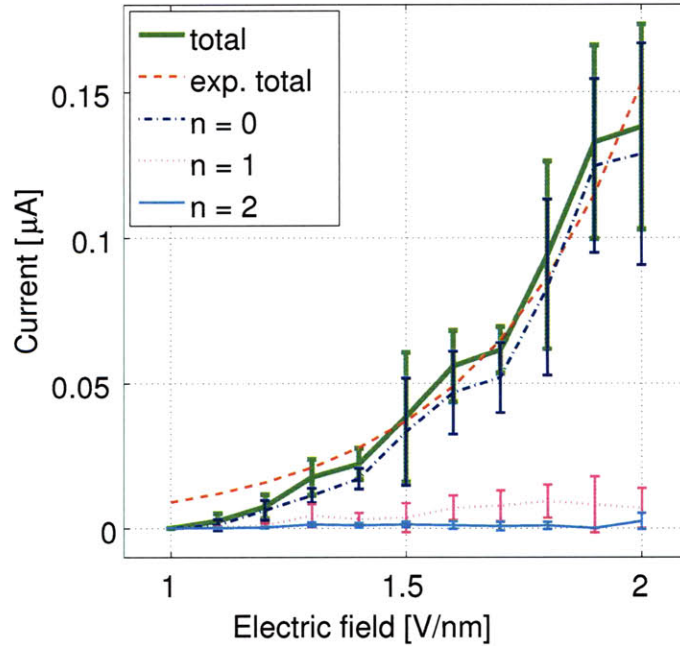
(b) $(EMI\text{-}BF_4)_n BF_4^-$

Figure 7-2: Current profile for (a) positive and (b) negative sides in various applied E fields.
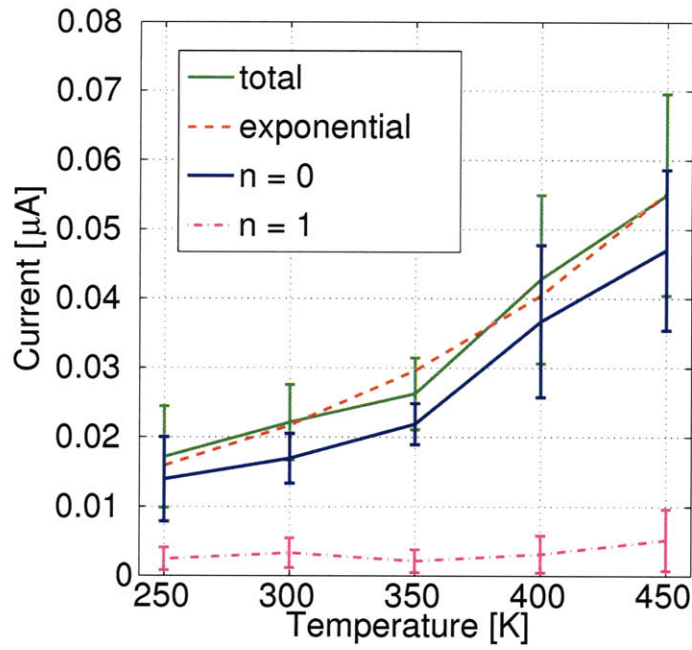
(a) $(\text{EMI-BF}_4)_n\text{EMI}^+$
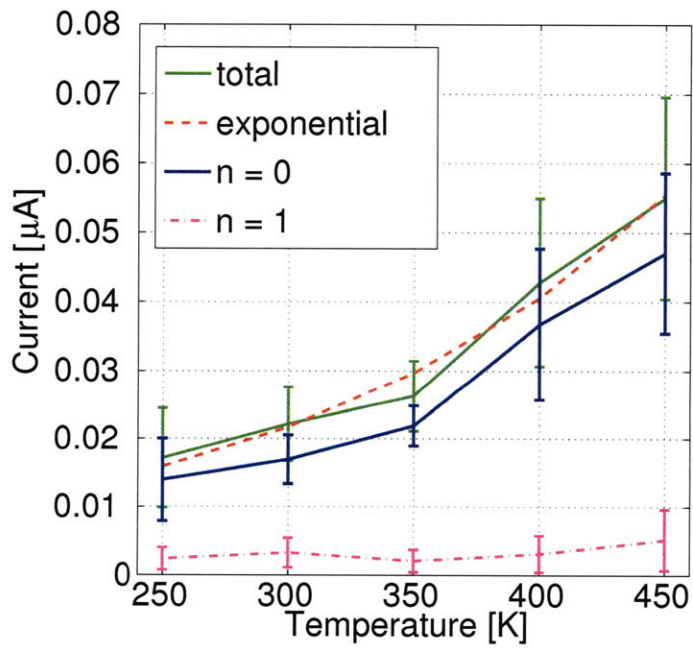
(b) $(\text{EMI-BF}_4)_n\text{BF}_4^-$

Figure 7-3: Current profile for (a) positive and (b) negative sides in various temperature with electric field 1.4 V/nm.

7.2 Local electric fields

Local electric fields are different from applied electric fields due to space charge distribution in the droplet. In order to investigate the difference, the local electric field experienced at the position at an extracted ion is estimated through the superposition of the contribution of each individual point charge and the applied electric fields.

$$\vec{E} = \vec{E}_{spacecharge} + \vec{E}_{external} \tag{7.1}$$

and

$$\nabla \bullet \vec{E} = \frac{\rho}{\epsilon_0} \tag{7.2}$$

Example of local electric fields along x, y and z directions are shown in figure 7-4 and 7-5, respectively. In this case, the externally applied field is directed along x only. The local electric field is tracked from the beginning of the simulation until the followed ion is emitted and leaves far enough until the electric fields from charges in the droplet become negligible. The center of mass of the target ion is used for the calculation and all partial charges of every atom are considered, except those of the followed ion. Before emission occurs, the ion is exposed to strong negative electric fields from its surroundings and is kept inside the droplet while the field magnitude decreases throughout the relaxation process. As for ion emission, in a macroscopic sense, it is not possible to measure such localized phenomena. Ions leave from a droplet when the local electric field in the x direction reaches its highest value, while highest values along y and z do not always happen when E_x is largest. The Schottky model relies on a statistical ensemble and therefore applies to macroscopic phenomena. The microscopic details described here are very peculiar to the atomistic analysis.

(a) x direction

(b) y direction

(c) z direction
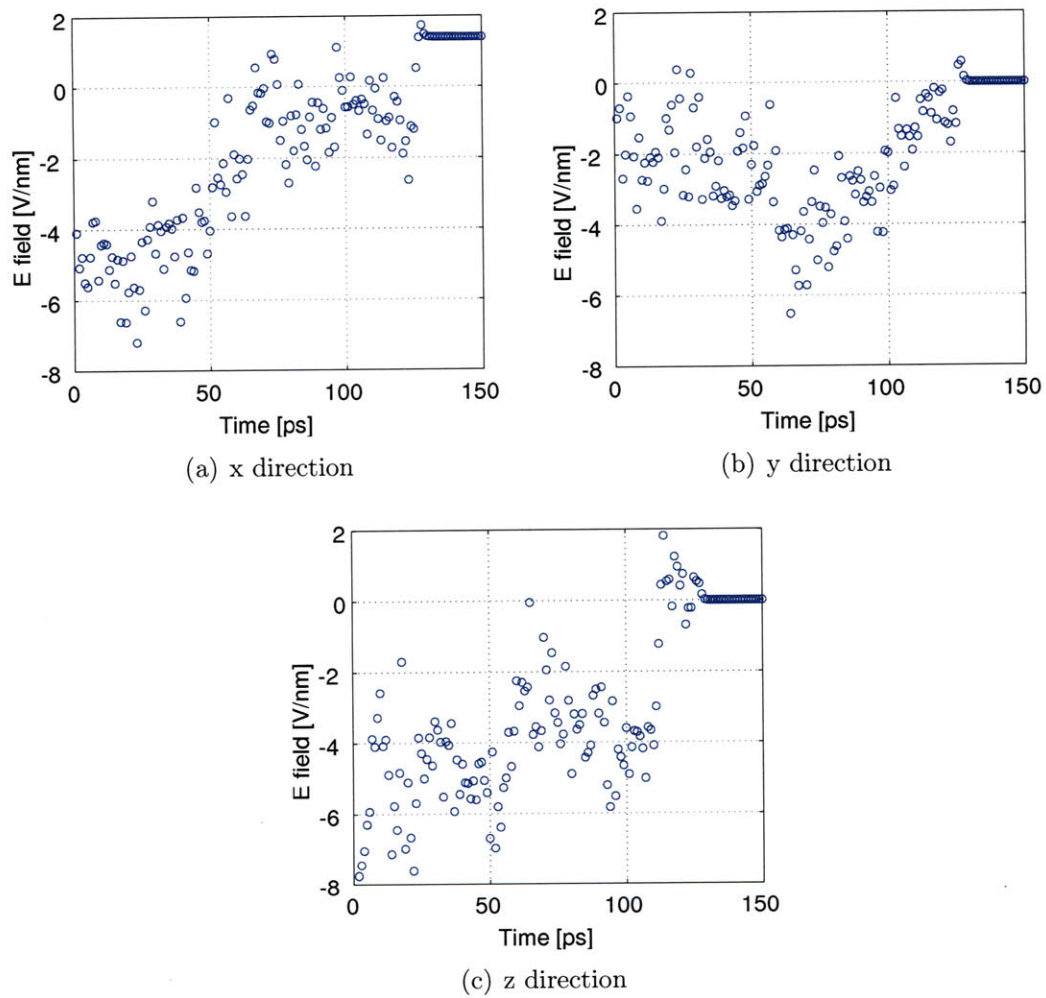
Figure 7-4: Local electric fields on a positive emitted ion in three dimension at the applied electric field 1.4 V/nm.

60

(a) x direction

(b) y direction

(c) z direction
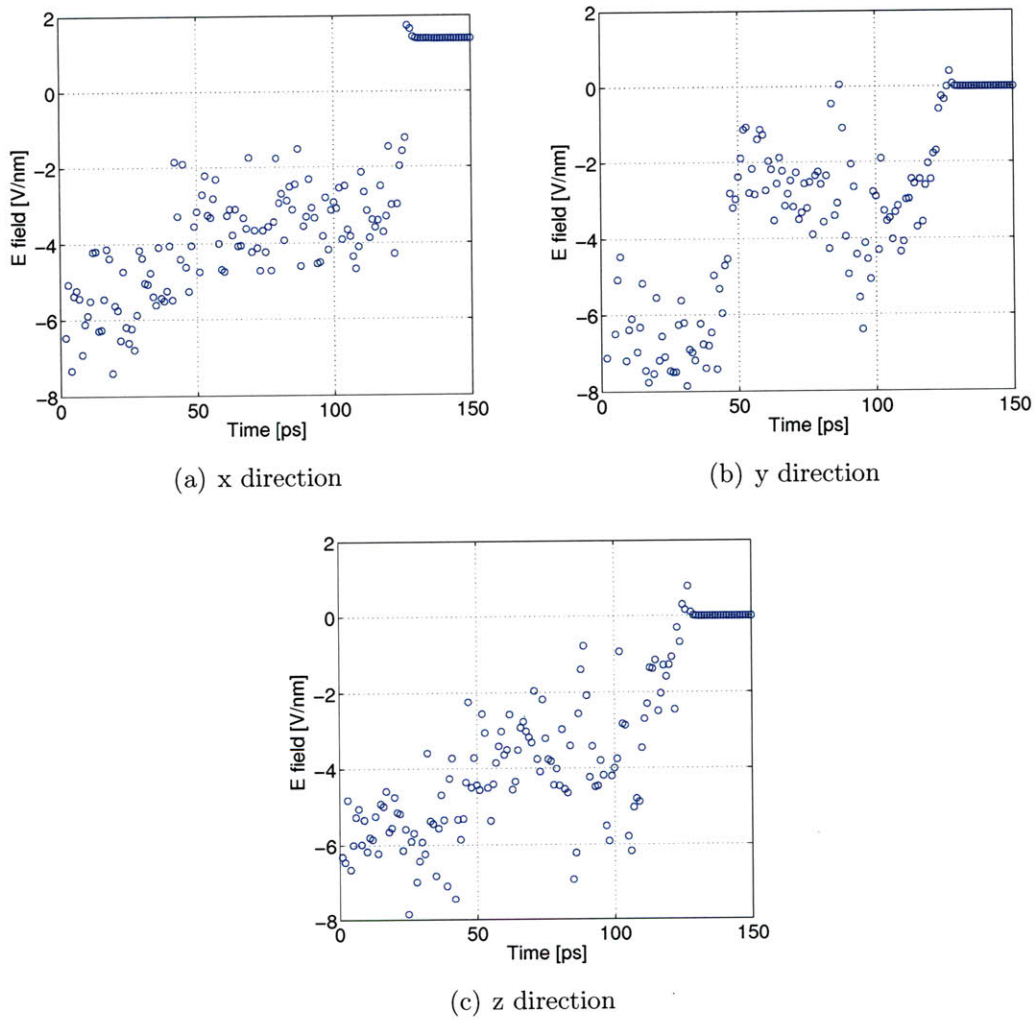
Figure 7-5: Local electric fields on a negative emitted ion in three dimension at the applied electric field 1.4 V/nm.
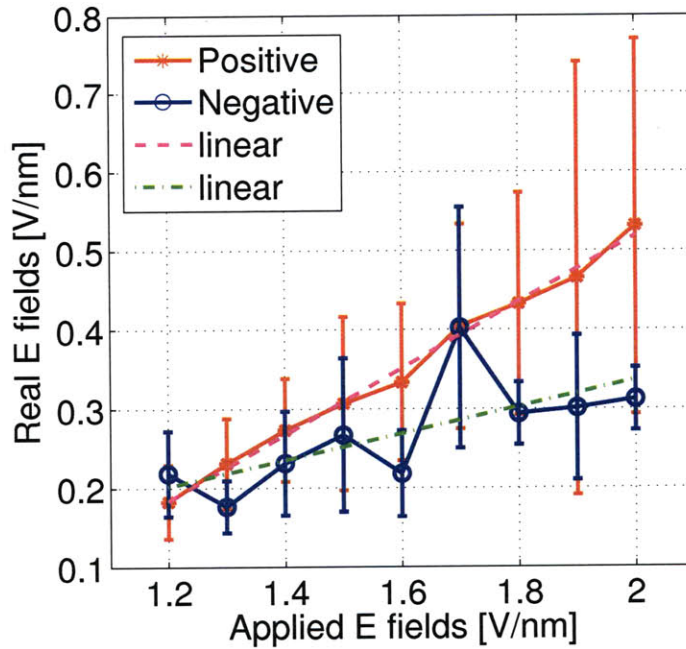
Figure 7-6: Local electric field vs. applied electric field at the point of ion emission in 300K

To investigate the trends of local electric fields at the point of ion emission in terms of various applied electric fields, the local electric fields are taken as the average of five samples obtained by root-mean-square of the electric field magnitude in all three x, y and z directions. The local electric fields are compared to the applied electric fields as shown in figure 7-6. Local electric fields are smaller than applied electric fields for both positive and negative ions. Though the number of extracted ions is similar between positive and negative sides, it can be seen that positive ions (EMI) locally require higher electric fields probably because of the unsymmetrical shape of the cation. In the experiment by Hogan et al. [67], the activatoin energies differ by approximately 0.25eV.
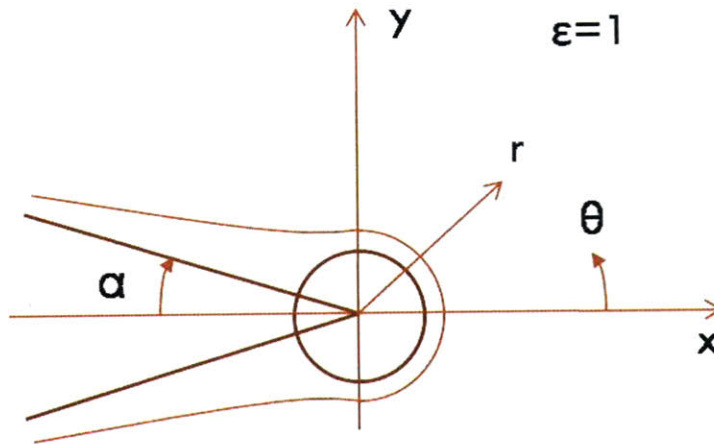
Figure 7-7: Schematic of sphere on cone model

7.3   Estimation of propulsive properties

Propulsive properties of electrospray thrusters are estimated using the current and electric fields relationship shown in figure 7-2 [68].

We assume the existence of a Taylor cone [1] with ion emissions issuing from its apex. The electric field distribution along a Taylor cone surface is inversely proportional to $\sqrt{r}$, where r is the distance from the tip along the surface. Thus, ion evaporation could occur not only from the very tip of the cone, but also from adjacent regions upstream from the tip, provided the field is strong enough. By definition, a Taylor cone has infinite curvature at its apex. In real electrospray sources, such a cone is an idealization which is only accurate far away from this singularity. Instead of an ideal sharp point, the tip has some finite radius of curvature that dictates the strength of the field. The radius of curvature is a function of electrostatic and liquid properties, such as the applied voltage, electrical conductivity and surface tension. To account for the rounded apex at Taylor cone, the electric distribution on the liquid surface is obtained from the sphere on cone (SOC) model [69],[55].

In the SOC model, the equipotential lines are found by solving the Laplaces equation, $\nabla^2 \Phi = 0$ in spherical coordinates. The potential distribution is;

$$\Phi = -V \frac{\left(\dfrac{r}{a}\right)^{\nu} - \left(\dfrac{a}{r}\right)^{\nu+1}}{\left(\dfrac{D}{a}\right)^{\nu} - \left(\dfrac{a}{D}\right)^{\nu+1}} P_\nu(cos\theta) \tag{7.3}$$

Here, P_ν is the Legendre function of order ν. From this potential distribution, the electric field is derived,

$$\vec{E} = -\nabla \Phi \tag{7.4}$$

$$= -\frac{\partial \Phi}{\partial r}\vec{i_r} - \frac{1}{r}\frac{\partial \Phi}{\partial \theta}\vec{i_\theta} \tag{7.5}$$

where,

$$E_\theta = -\frac{\partial \Phi}{\partial r} \tag{7.6}$$

$$= \frac{V}{r_m}\left(\frac{r_m}{D}\right)^{\nu}[\nu + (\nu+1)f^{-2\nu-1}]P_\nu(cos\theta) \tag{7.7}$$

$$\tag{7.8}$$

$$E_r = -\frac{1}{r}\frac{\partial \Phi}{\partial \theta} \tag{7.9}$$

$$= \frac{V}{r} \frac{\left(\dfrac{r}{a}\right)^{\nu} - \left(\dfrac{a}{r}\right)^{\nu+1}}{\left(\dfrac{D}{a}\right)^{\nu} - \left(\dfrac{a}{D}\right)^{\nu+1}} \frac{d}{d\theta}[P_\nu(cos\theta)] \tag{7.10}$$

Here, $r_m = fa$ is the radius of the meniscus, where f is a factor that determines the surface equipotential and a correspondes to the model sphere radius. It can also see that the applied voltage is necessary to obtain the surface electric fields.

Equation 7.8 is used for the Legendre polynomial considering the limit of our target x and ν (-1< $cos\theta$ <1 and 0< ν <1).

$$P_\nu(x) = \sum_{n=0}^{\infty}(-1)^n \frac{(\nu - n + 1)\dots\nu\dots(\nu + n)}{(n!)^2}\left(\frac{1 - x}{2}\right)^n \tag{7.11}$$

$$(\nu > 0, -1 < x \leq 1) \tag{7.12}$$

Once the equipotential lines are obtained for a selected applied voltage between the tip and extractor, the equipotential line whose angle relative to the x axis is approximately 49 degrees is selected as the Taylor cone surface model. Then the electric field on such equipotential line is found by equation 7.5 and used for the distribution along the cone surface. This electric field distribution dictates the level of ion evaporation from the Taylor cone surface and establishes the individual ion statistics for each electric field.

In estimating the thrust, velocities are measured when the emitted ions are 20-40 nm far from the droplet in the direction of the electric field. This distance is not arbitrarily chosen. In a true electrospray system, the field amplitude drops off dramatically with distance, yielding an equally pronounced acceleration amplitude decay. In the MD simulation system, the ions are accelerated by constant electric fields. Here, we assume that this 20-40 nm artificial distance is equivalent to the approximate terminal velocities in its physical correlate, even though weaker field keeps accelerating the ions through longer distances in a real system. The solvated ion break up is taken into account for the thrust on both the positive and negative sides. Because some of the solvated ions appear to be in a metastable state, breakup of solvated ions cause fewer accelerated ions.[54] Once the solvated ion breaks into a neutral(s) and a bare ion, only the ion is accelerated. Neutral ion emissions are
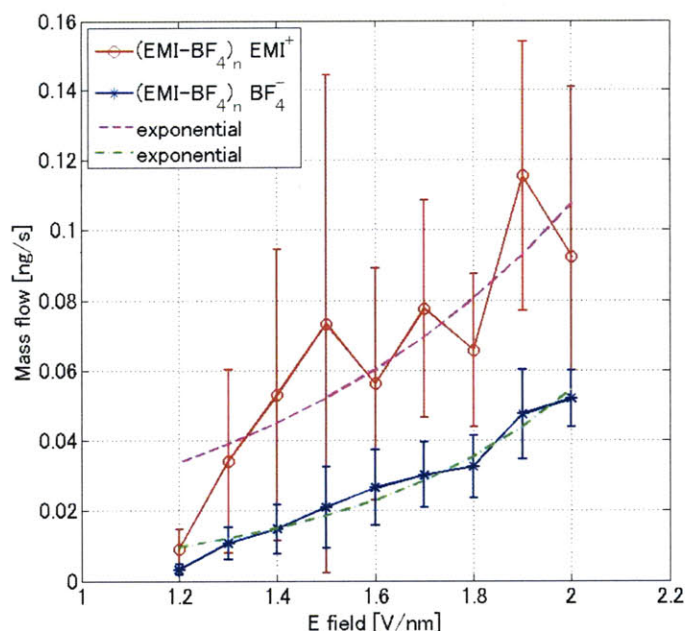
Figure 7-8: Mass flow from droplet

not included in the thrust. The thrust density is given as the thrust divided by one half of the surface area of the droplet. The area is approximately 27 nm^2. The mass flow from the droplet is measured and related to total mass flow from the surface of the Taylor cone. Data from five different initial conditions are averaged out for electric fields from 1.2 to 2.0 V/nm. In previous studies, it was found that solvated ion emission is rarely observed above 2.0 V/nm and ion emission does not occur below 1.1 V/nm, at least within the simulation time.[76]

Based on the ion evaporation analysis using the MD simulation, the number of emitted ions in each electric field is between 20 and 40 in both positive and negative polarities. After ions have been emitted by this amount, the droplet itself loses its consistency and breaks up.

The thrust from the droplet is shown in Figure 7-9. The thrust from (EMI-BF$_4$)$_n$BF4$^-$ is smaller than (EMI-BF$_4$)$_n$EMI$^+$ because of the mass difference. As expected, thrust increases with stronger electric fields. Mass flow from the droplet is shown in Figure 7-8. The mass flow of positive ions is relatively random compared

66
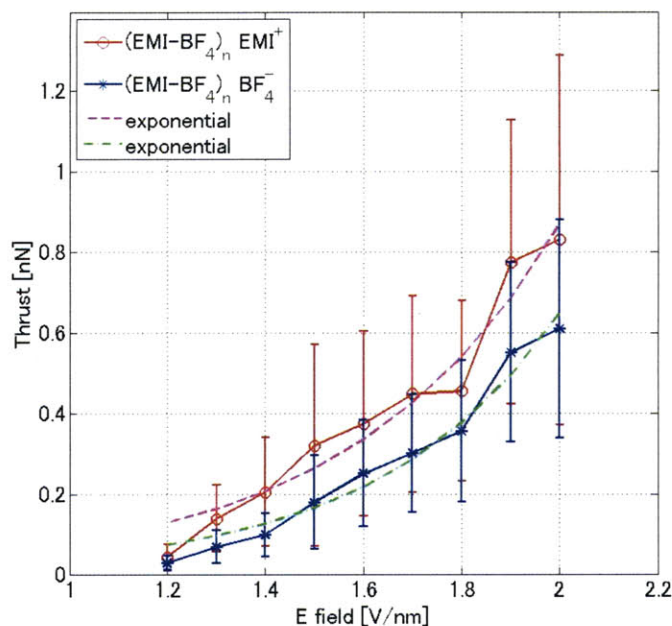
Figure 7-9: Thrust from droplet

to the negative polarity. This tendency can be seen even considering ion break-up because the fraction of solvated ions is small when the ion evaporations occur at more than 1.3 V/nm. The fraction of the solvated ions appear in Figure ??. The total current is dominated by bare ions, and current by solvated ions remain low even under stronger electric fields.

Figures 7-12, 7-10 and 7-11 show the calculated thrust, Isp and current from the Taylor cone when 2.5 to 3 kV are applied between the needle and extractor. These values are approximately on the same order at same experimental results. [52],[70]

Because thrust is dominated by bare ions and mass flow is not affected significantly by the breakup of solvated ions, it can be said the results reflect an emission of mainly intact solvated ions even in strong constant electric fields. The reason why the breakup is hard to occur and why the number of emitted solvated ions is small might relate to the force field difference between the stationary state and under strong electric fields. A more accurate quantum model would be required to dynamically characterize the charge distributions of the emitted ions. Such approach would be

important to establish the metastability of solvated ions.
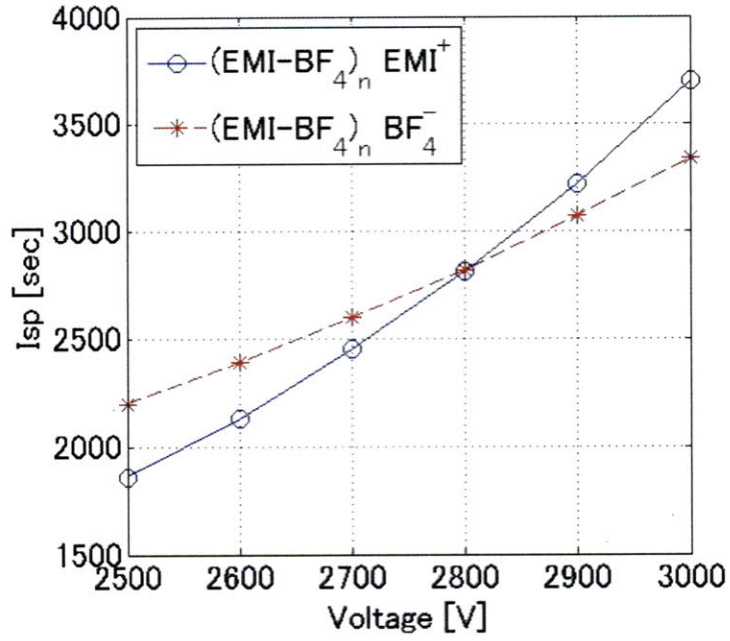
Figure 7-10: Estimated Isp from Taylor cone
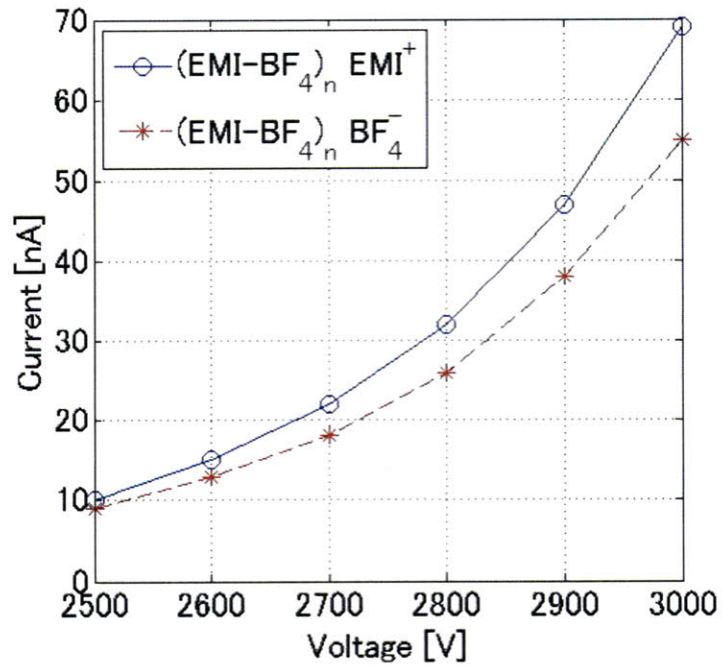
Figure 7-11: Estimated current from Taylor cone

69
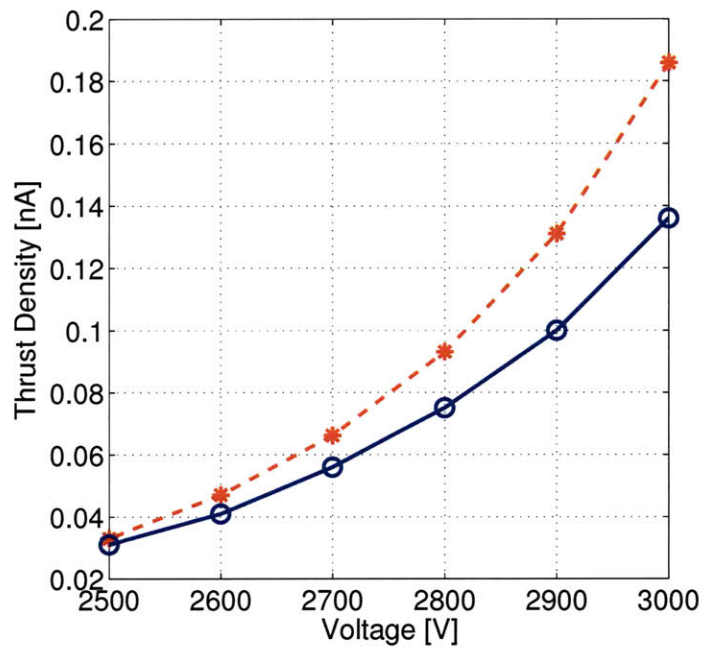
Figure 7-12: Estimated thrust from Taylor cone

7.4 Activation energy analysis

7.4.1 Schottky model

The activation energy, or the free energy of the field evaporation process is estimated using a Schottky-type model [24]. In equilibrium, the field-enhanced thermionic emission of charged particles is described by,

$$j = \sigma \frac{kT}{h} exp \left[-\frac{1}{kT} \left(\triangle G_0 - \sqrt{\frac{e^3 E}{4\pi\epsilon_0}} \right) \right] \tag{7.13}$$

where σ, k, T, h and $\triangle G_0$ are the surface charge density, Boltzmann constant, temperature, Planck's constant and activation energy, respectively. The second term inside the exponential is commonly known as the Schottky depression and represents the amount by which the surface-ion interaction barrier is decreased due to the presence of an electric field. This expression is derived from statistical physics arguments in equilibrium and is therefore valid for aggregate systems formed by a large number of particles. Nevertheless, in the same spirit that the statistical identity of a given system can begin to be observed with a reduced number of particles (in quantum statistics, for example, by finding the form of the most probable distribution), the nano-droplet system composed of a few thousand atoms is sufficiently large for this expression to be applied with an acceptable degree of confidence. To obtain a numerical value of the activation energy, Equation 7.13 is compared against an exponential fit of the total emitted current density as a function of temperature from 250K to 450K and a fixed electric field with a magnitude of 1.4 V/nm which is shown in section 7.1.

The exponential fit is used to match the equation from the Schottky model 7.13 to estimate the activation energy in this section.

7.4.2 Droplet energy

To take advantage of the discrete nature of MD simulations, the activation energy is also examined by keeping track of the droplet energy before and after a particular ion

is emitted. It is examined that the temperature of droplet remains constant during the emission process.

We assume the kinetic energy acquired by flying ions does not modify in an appreciable way the internal energy of the system. Therefore, as an approximation, changes in the droplet energy are only related to changes in the interaction potentials within the atoms that make up the droplet and the field evaporated ions. The potential energies include covalent bond, LJ and Coulomb interactions. The droplet energy is expected to change by a certain amount when an ion is extracted. This energy change is directly related to the activation energy (or the free energy for an open system, $dG|_{T,P} = \sum \mu_i dN_i$, where μ_i is the chemical potential and N_i the number of particles for species i), at constant pressure and temperature. This approach to estimate the activation energy includes the contributions of the different interaction potentials in a direct way. Upon ion emission, Coulomb and van der Waals forces practically vanish between atoms in the droplet and the extracted ion. The extracted ions include both non-solvated and solvated ions.

Energy profiles of potential energy of droplet are obtained against time. The approximate activation energy is derived from the slope of energy vs. time characteristics and the number of emitted ions per unit time. This activation energy represents the average energy change of every ion emission. The analysis of activation energy is done using applied electric fields from 1.2-2.0 V/nm for five different initial conditions. To obtain the activation energy, the potential energy of the droplet tracked during ion emission. One example of an energy profile is shown in figure 7-13 This represents the droplet's potential energy under an electric field of 2.0 V/nm encompassing the extraction of four negative ion emission and three positive ions. The activation energy is approximated by the slope of the energy during the emission time interval. However, due to the strong imposed electric field, the droplet deforms with an effective reduction of the activation energy. Thus, we took only the first 5-6 ions to obtain the activation energy to avoid strong deformations. The results are shown in figure 7-14. These data are averaged over five different initial conditions. The experimental data show that nano droplets of EMI-BF$_4$ gives activation energies of 1.83 [eV] and 1.58
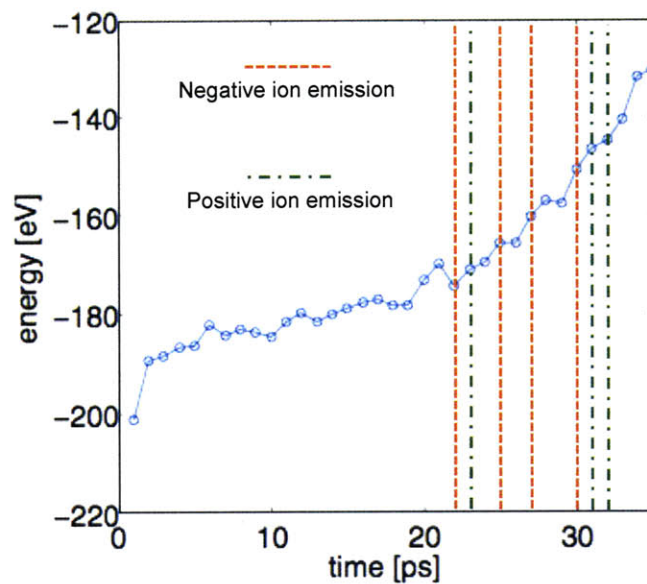
Figure 7-13: Droplet potential energy under electric field of 2.0 V/nm

[eV] for negative ions and positive ions respectively. [67] From figure 7-14, activation energies at 1.2, 1.3 and 1.4 [V/nm] give 1.5 times higher values than other cases. However the other values provide around 1.8 eV which is a reasonable value when compared with experiments, though further investigation is necessary to make sure whether higher activation energies is real or is introduced as an artifice of the model.
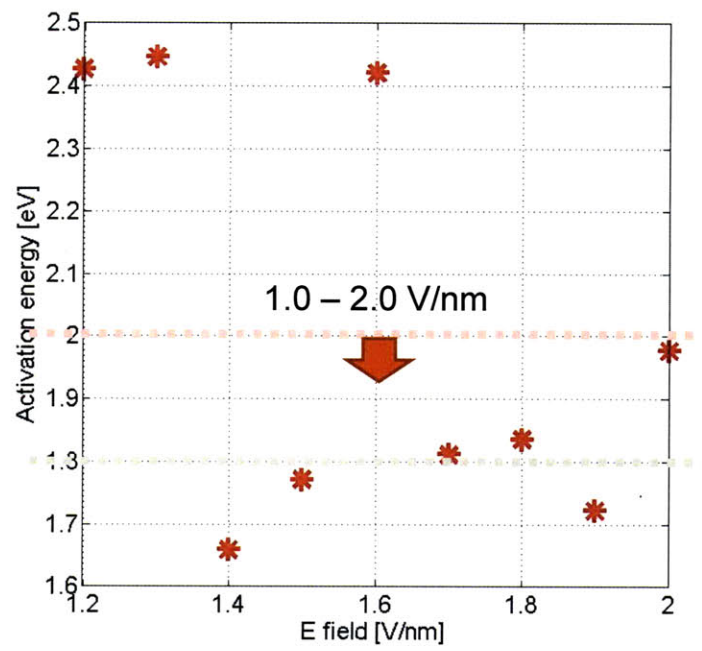
Figure 7-14: Activation energy from droplet energy

Chapter 8

Ion Evaporation by Internal Fields

8.1   MD Approach to High Internal Electric Fields

Based on the Rayleigh limit argument, ion emission before coulomb fission was investigated using MD simulations. Coulomb fission happens when charges find a droplet force the the balance between electrostatic and surface tension of the liquid near the limit of stability.

The electrostatic pressure for a fully relaxed charged sphere is,

$$P_E = \frac{\sigma^2}{2\epsilon_0} \tag{8.1}$$

where σ is the surface charge density and ϵ_0 is the permittivity of vacuum.

The surface tension pressure of the liquid droplet in vacuum with the spherical radius R is,

$$P_R = \frac{2\gamma}{R} \tag{8.2}$$

where γ is the surface tension.

Rayleigh instability occurs when the values of equation 8.1 and 8.2 become equivalent.

$$q_R = \sqrt{8\pi^2 \epsilon_0 \gamma d^3} \qquad (8.3)$$

The electric field strength at the droplet surface in the absence of an external field is,

$$E = \frac{q}{\pi \epsilon_0 d^2} \qquad (8.4)$$

and the critical field is from equation 8.3 and 8.4,

$$E_R = \frac{q_R}{\pi \epsilon_0 d^2} > E_{ion} \qquad (8.5)$$

where

$$E_{ion} = \frac{4\pi \epsilon_0 \triangle G_0^2}{e^3} \qquad (8.6)$$

This indicates that the Coulomb fission occurs under certain internal electric field and the electric field for the fission has to be larger than the E field for ion evaporation.

To investigate the energy required for the ion evaporation, we model this condition avoiding the fission using MD simulation removing ions from a nano-droplet and therefore forcing droplet charging. The droplet contains 64 EMI-BF$_4$ molecules and BF$_4$ ions are removed one by one until ion emission is observed. To achieve this we:

1. Equilibrate the droplet following the same steps shown in section 6.2 for three different initial conditions at each temperature (300, 323 and 272 [K]).

2. Remove one BF$_4$ ion from the last step of the previous simulation and run a new simulation using the NVT ensemble until the new droplet reaches equilibrium.

3. Check for ion emission. If the emission is observed, stop the simulation and restart the last simulation using the NVE ensemble. If ion emission is not observed, repeat from step two.

Equilibrium is checked by the stabilization of the total energy, which is sum of

energy of pair and intra molecular potentials. As for visualization of the MD result, Visual Molecular Dynamics (VMD) [71],[72] is used for the ion emission observation.

8.2 Activation Energy Analysis as a Function of Temperature

One case of simulation results is shown in figure 8-1. Steps represent ions removed, with the energy difference mainly caused by breakup of electrostatic bonds.

To verify this point, we estimated the energy reduction per unit volume of a droplet when a single ion is removed. [37]

$$\frac{Energy}{Volume} = \frac{1}{2}\epsilon_0 \left(\frac{e}{4\pi\epsilon_0 R^2}\right)^2 \tag{8.7}$$

using the volume of a sphere,

$$Energy = \frac{1}{2}\left(\frac{e}{4\pi\epsilon_0 R^2}\right)^2 \frac{4}{3}\pi R^3 \epsilon_0 \tag{8.8}$$

converting unit to [eV],

$$Energy_{[eV]} = \frac{1}{24}\frac{1}{\epsilon_0\pi}\frac{e}{R} \approx 0.24[eV] \tag{8.9}$$

Now, converting the energy unit in figure 8-1, using 100 [g/mol] as an average mass of EMI (111 [g/mol]) and BF_4 (87 [g/mol]), the energy step (approximately 150 kcal/mol) is 0.197 [eV], which is close to the value in equation 8.9.

Table 8.1: Number of ions removed when ion emission occurs

Initial condition types	300K	323K	373K
ver.1	8	7	7
ver.2	7	7	7
ver.3	8	8	7

The table 9.1 shows the number of ions removed when ion emission occurs. For all temperatures, ion emission is observed when 7 or 8 ions are removed. Although

77

the energy profile also includes the emitted ion's kinetic and potential energy, the large energy drop represents that the pair potential, specifically the Coulomb force, is strong enough compared to the emitted ion energies. These emissions are not only for single ion emission, but also for solvated ion emission and even droplet breakup as shown in figure 8-2. Here, the energy drop for each emission type takes almost the same value (150 kcal/mol).

In order to investigate ion emission without a thermostat, NVE simulations are conducted for the sequence at which ion emissions are observed in the NVT simulations. Here, the total energy is nearly constant, therefore pair potential energies are checked for the energy profile. Ion emission exist in all initial conditions/temperatures and we could see energy drops for ion emission similar to the NVT cases (figure 8-4).

(a) 300K

(b) 323K

(c) 373K
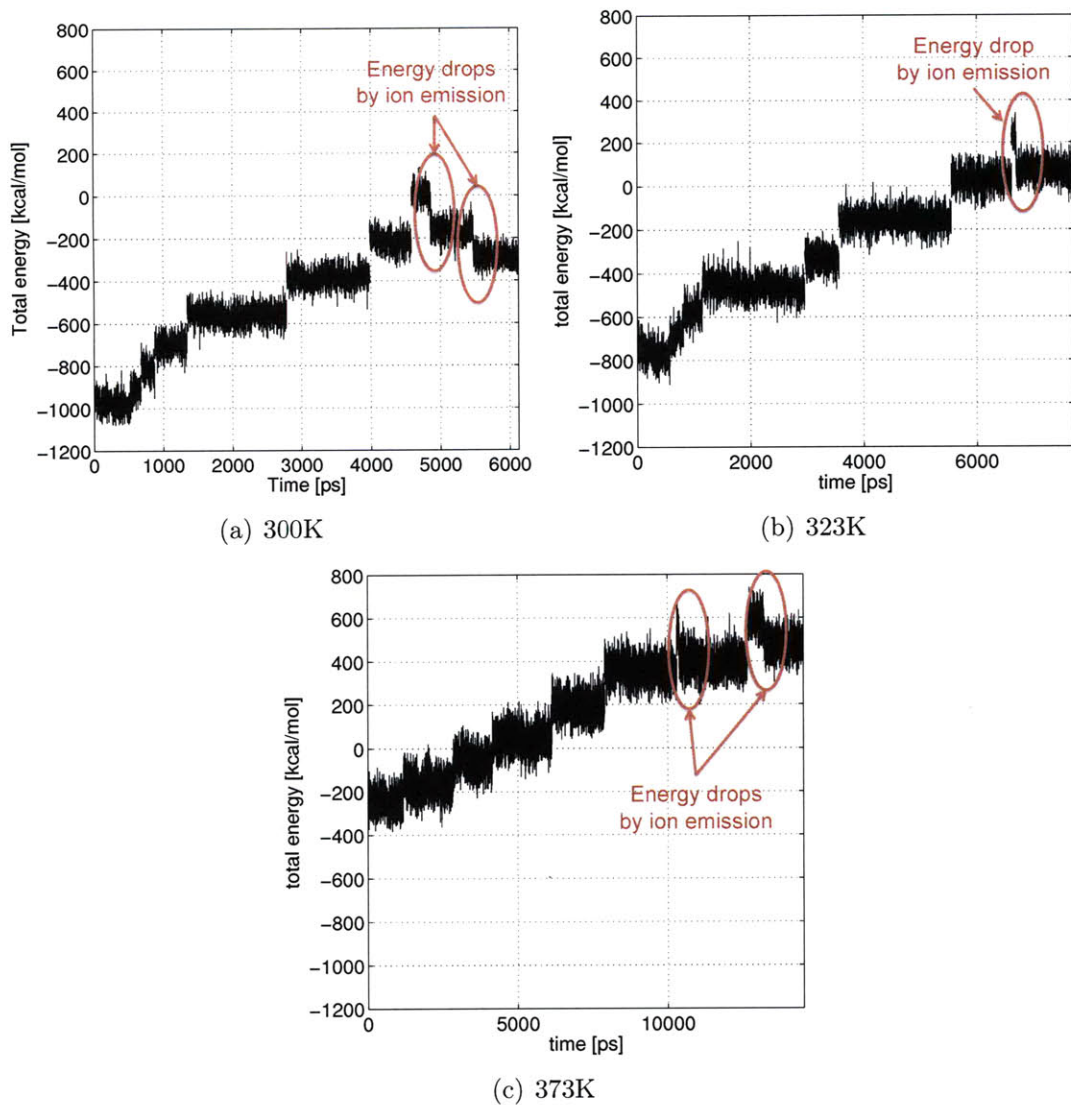
Figure 8-1: Total energy profiles for ion removed simulations (Initial condition version 1.)

(a) Droplet breakupVer.2 373K: 7 BF_4 removed

(b) Single ion emission, Ver.3 300K: 8 BF_4 removed

(c) Solvated ion emission, Ver.1 300K: 8 BF_4 removed

Figure 8-2: Ion emission types
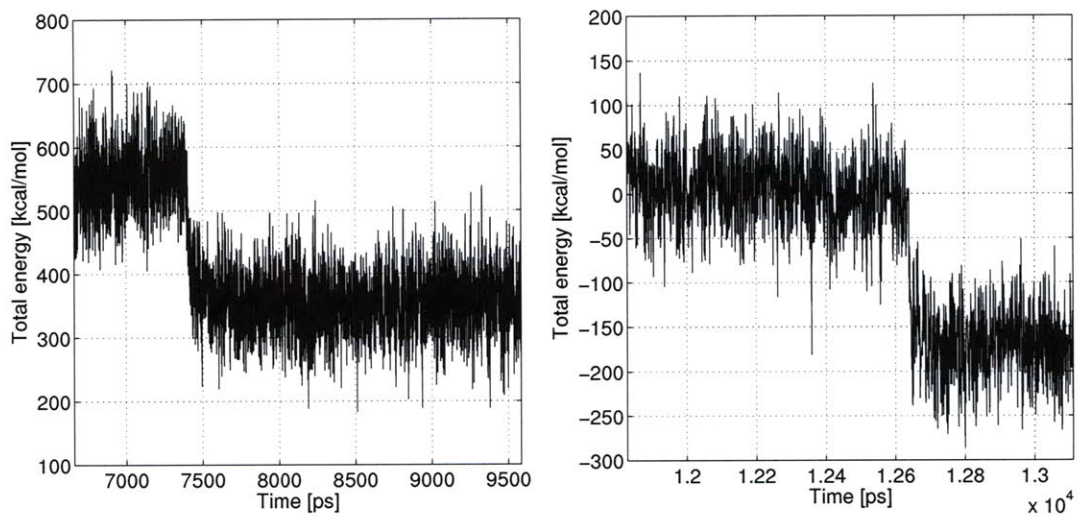
(a) Droplet breakupVer.2 373K: 7 BF$_4$ removed

(b) Single ion emission, Ver.3 300K: 8 BF$_4$ removed
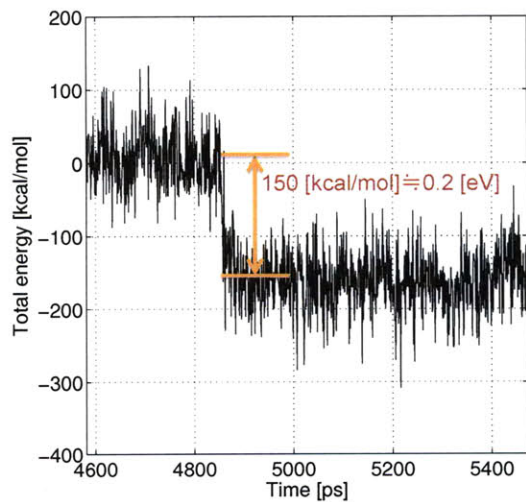
(c) Solvated ion emission, Ver.1 300K: 8 BF$_4$ removed

Figure 8-3: Total energy profile at the sequence when ion emission is observed. Each figure corresponds to figure 8-2.
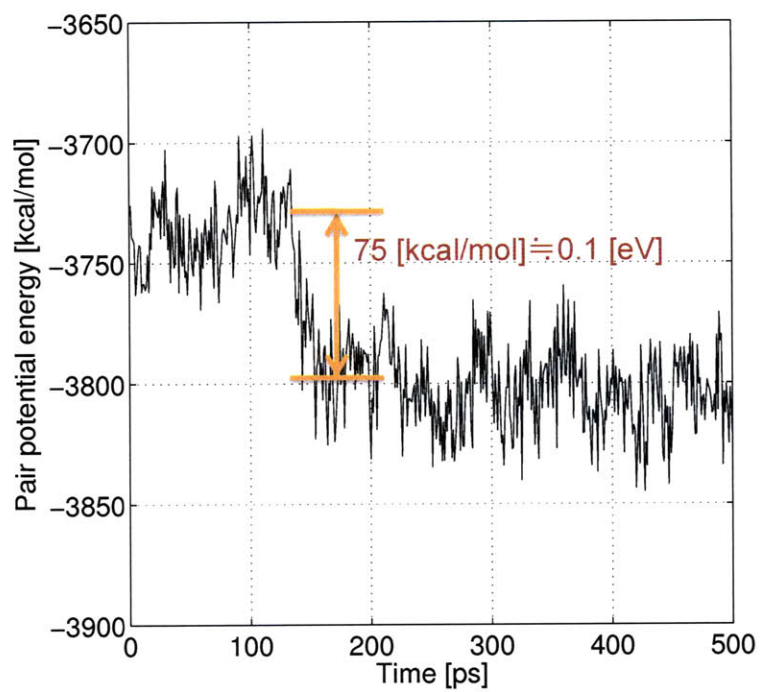
Figure 8-4: Pair potential energy profile of ion emission in NVE ensemble: ver.1, 8 BF$_4$ removed at 323K

Chapter 9

Interaction between Solid Plate and Liquid Droplet

9.1 Computational Model

One final model includes an EMI-BF$_4$ droplet and a tungsten plate (figure 9-1). This flat tungsten plate represents the preliminary simplified model for the electrospray emitter. The size of the tungsten plate is changed depending on the total number of molecules. The initial coordinates for the simulations with high electric fields are obtained from the equilibrium state at near room temperature $T = 300$ K. The details of the equilibrium process are discussed in section 9.4 and 9.5.

The force field of EMI-BF$_4$ is same as before and for the tungsten plate, we assume the interactions are of the Lenard-Jones (LJ) type, with a Body Centered Cubic (BCC) configuration. For the tungsten atoms, we use the force field parameters suggested by Tanaka et al.[73].
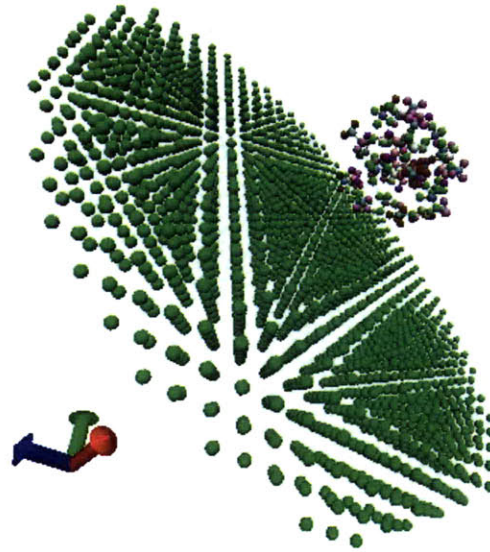
(a) Atomistic model of tungsten and EMI-BF$_4$ droplet
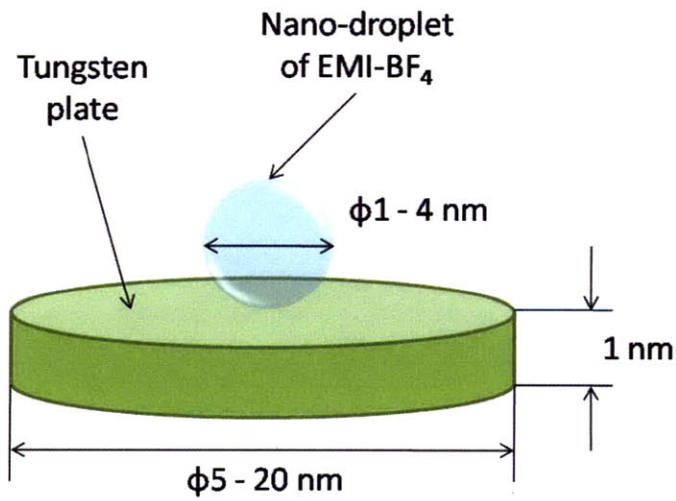
(b) Dimension of model with the tungsten and 8 mol EMI-BF$_4$ droplet

Figure 9-1: 3D structure of the model with tungsten and EMI-BF$_4$ droplet

9.2   MD simulation methodology

The following are the steps for used for the MD simulation.

1. Equilibration of system

   (a) Equilibration of a nano-droplet of EMI-BF$_4$ with NVT ensemble.

   (b) Equilibration of tungsten and the nano-droplet with NVE ensemble.

2. Simulate the system under electric field conditions.

   - Apply constant and uniform electric field to the system.

   - Apply surface charge on the top layer of the tungsten plate.

For the first step 1(a), EMI-BF$_4$ molecules are placed arbitrary in a cubic configuration as an initial condition. Once the MD simulation is started, the cubic configuration gradually transforms to a spherical shape. The diameter of the droplet depends on the number of EMI-BF$_4$ molecules. It is approximately 1 nm to 2 nm for 8 and 27 EMI-BF$_4$ molecules, respectively. This simulation is conducted with the NVT ensemble for 300 K using the Nóse-Hoover thermostat[64] with a temperature damping of 100 K. The cutoff distances are 8 Å and 100 Å for LJ and Coulombic potentials, respectively. The time step is 1 fs and the maximum total simulation time is 50 ns which corresponds to 50 million iterations. The periodic boundary condition is not used because this is an isolated floating system. The completion of equilibration is checked both by visualization and energy profiles. After the equilibrium is reached with the NVT simulation, the final trajectory of 1(a) is used for the initial condition of 1(b). Here, the tungsten plate is added to the system and the distance between the nano-droplet and the plate is set to approximately 3 Å. The initial condition of the tungsten plate has BCC configuration with a lattice constant of 3.165 Å. This tungsten plate initial configuration is obtained by several trials using different shapes. The details are in section 9.5.

Once the equilibration is achieved in step 1(b), the tungsten and the nano-droplet are exposed to electric fields. We investigated two types of electric field circumstances

as mentioned above. The former model provides a simpler configuration and has been discussed in several studies.[74], [75], [76] However, because it is only consistent with a realistic model very near to the surface, we consider also a model using surface charges, which gives a decaying electric field which is more realistic. The details of the surface charge approach are discussed in section 9.2. The constant electric field is applied perpendicular to the surface of the tungsten plate. In these calculations, the position of all tungsten atoms are fixed due to the severe computational cost that otherwise would arise. Also, to make the simulations faster, a neighbor list is applied. The skin distance for the neighbor list is set to 10 Å. A shrink wrapping algorithm is used for ion emission which have a possibility of leaving the simulation box. The boundary conditions are not periodic in this calculation, either, and the ensemble is NVE with a time step of 1 fs. The initial temperature is 300 K.

9.3   Surface Charge on Tungsten Plate

To simulate a charge distribution, charges are applied to atoms on the top layer of the tungsten plate, such that

$$\sigma_{sur} = \frac{Q}{S} = \epsilon_0 E \tag{9.1}$$

where $\sigma_s ur$, Q, S, ϵ_0 and E are surface charge, total charge on the surface, surface area, permittivity and electric field, respectively. The area is obtained from the lattice constant as shown in figure 9-2. Here,

$$Q = Nq \tag{9.2}$$

where N and q are the number of atoms at the top layer of the tungsten plate and charge on each atom, respectively. Therefore, the charge for each atom is

$$q = \frac{\epsilon_0 A}{N} E \tag{9.3}$$

This amount of charge is applied to provide an electric field E on the surface. The
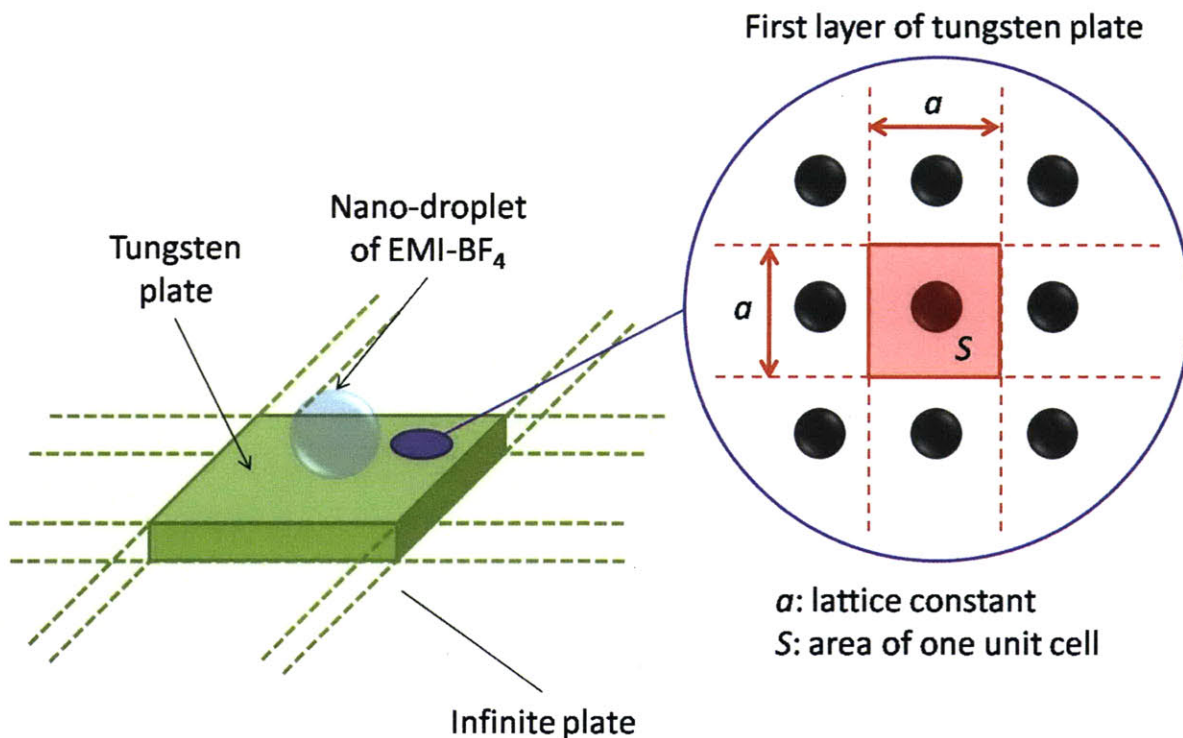
Figure 9-2: Schematic of the first layer of the tungsten plate.

electric field is varied to observe ion emission of EMI-BF$_4$.

It is important to point out that a uniform charge distribution on the finite simulated plate does not produce an equipotential surface and as a consequence the corresponding field is not necessarily normal to the surface. This is a good approximation only if the size of the plate is much larger than the size of the droplet, which is not the case of our simulations, mostly because of computational cost. In future work we plan to address this problem by incorporating periodic boundary conditions (see figure 9-2, left drawing) such that an infinite plate is simulated to produce a normal field from a uniform charge distribution.

9.4   Equilibration of Tungsten Plate

Because it is necessary to use LJ potential for the tungsten plate to calculate the interactions under non-periodic boundary conditions, there is a computational limi-

tation to the thickness of the tungsten plate. We tried several patterns to reduce the computational cost. The cutoff distance is 20 Å for LJ potential and the Coulombic force is not calculated because tungsten atoms are initially uncharged.

Figure 9-3 shows three examples of tungsten plates. The left figures (figure 9-3 (a), (d) and (g)) show model schematics, and the center (figure 9-3 (b), (e) and (h)) and right (figure 9-3 (c), (f) and (i)) figures correspond to snapshots of initial coordinates and time varying coordinates, respectively. The round model 1 (figure 9-3 (d), (e) and (f)) is built with a concept that provides a thick tungsten plate where the nano-droplet is placed while other parts have smaller thickness to reduce the number of tungsten atoms. The square model (figure 9-3 (a), (b) and (c)) and round model 2 (figure 9-3 (g), (h) and (i)) have uniform thickness of 3 lattices. It can be seen that the there are deformations in the square model and the round model 1. The deformation of the square model is not critical compared to the round model 1, however the number of atoms of the round model 2 are less than the square model. Also, the round model 2 perfectly keep its configuration as shown in figure 9-3 (h) and (i). Therefore we use the round model 2 for further simulations.

9.5 Equilibration of Tungsten Plate and EMI-BF$_4$ Nano-droplet

Equilibration of the tungsten plate and the EMI-BF$_4$ nano-droplet is done for two different system sizes with 8 and 27 molecules EMI-BF$_4$ droplet. The diameters of the tungsten plates are 8 nm and 10 nm, respectively. The total number of atoms are 2499 and 5343 for these systems. The combination of (a), (b) of figure 9-4 and 9-5 shows the initial condition and the equilibrated condition of 8 and 27 EMI-BF$_4$ molecules, respectively. Compared to the sole equilibration of droplets, these equilibrations need a longer cutoff distance for LJ potential because of the relatively large LJ coefficient of tungsten atoms. Here, we use 30 Å and 80 Å for 8 and 27 EMI-BF$_4$ molecules respectively. From figure 9-4 and 9-5, it can be seen that the equilibration condition
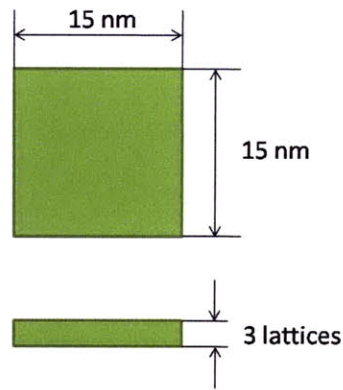
(a) Schematic of square model.   (b) Square model, 0 ps.   (c) Square model, 820 ps.
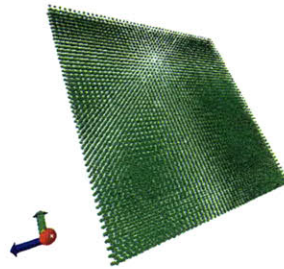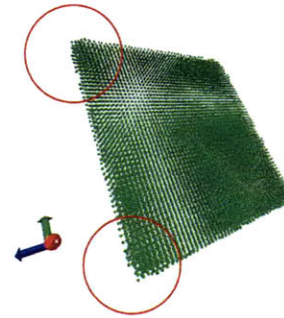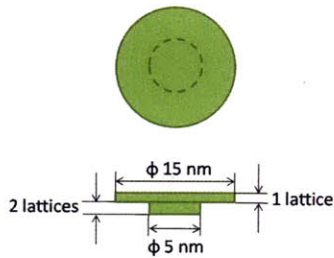
(d) Schematic of round model 1.   (e) Round model 1, 0ps.   (f) Round model 1, 1090 ps.
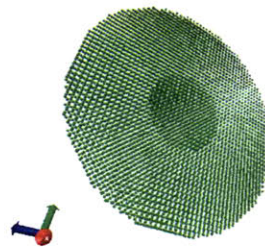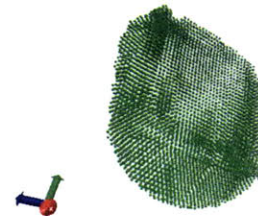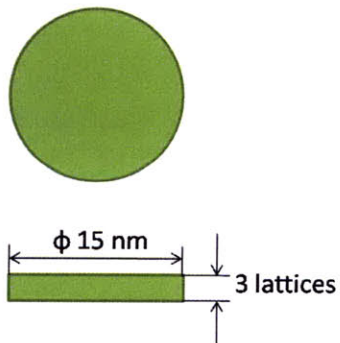
(g) Schematic of round model 2.   (h) Round model 2, 0 ps.   (i) Round model 2, 1110 ps.
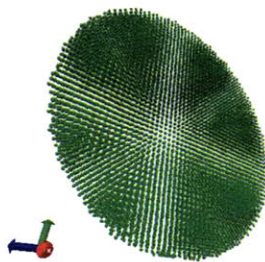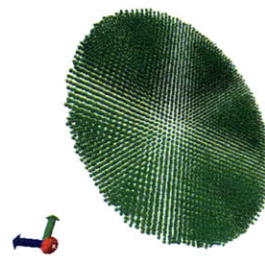
Figure 9-3: (a) (b) (c) Square model of tungsten plate. (d) (e) (f) Round model 1 of tungsten plate. (g) (h) (i) Round model 2 of tungsten plate

is totally flat and both EMI^+ and BF_4^- ions completely wetted the tungsten surface due to a strong attraction by tungsten atoms. For a more precise investigation of ion emission from a Taylor cone, a thicker liquid layer might be needed.

Figure 9-6 is the total energy profile throughout the equilibration runs. The 8-molecule system is equilibrated approximately at 50 ns, and the 27-molecule system converge at around 30 ns. The physical simulation time is 4 days for 350 ps in the 27 molecules case, even using a neighbor list and fixed tungsten atoms. Here, the force on tungsten atoms are not calculated and are set to zero. The most expensive part is the calculation of the LJ and Coulombic potentials with long cutoff distances. To study a larger system, it will be necessary to consider certain techniques such as the multiple time step method[77].

9.6 Tungsten plate and nano-droplet under electric fields

Here we investigate tungsten plate and nano-droplet under two sources of electric fields. Table 9.1 indicates the ion emission existence in four different conditions:

a. Ion emission under external constant electric field with 8 EMI-BF_4 molecules.

b. Ion emission with surface charge with 8 EMI-BF_4 molecules.

c. Ion emission under external constant electric field with 27 EMI-BF_4 molecules.

d. Ion emission with surface charge with 27 EMI-BF_4 molecules.

Figure 9-7 shows an EMI^+ ion emission from the 27-molecule system. The electric field is applied in the x direction which is perpendicular to the surface. Ion emission from an ionic liquid surface usually occurs in electric fields of 1.0 V/nm - 2.0 V/nm. However, here, the electric field needed for ion emission is higher than those values because ions are directly attached to the metal surface.

At electric fields stronger than 3.5 V/nm, ion emission along the x direction is observed under the external constant electric field condition, but no axial ion emission
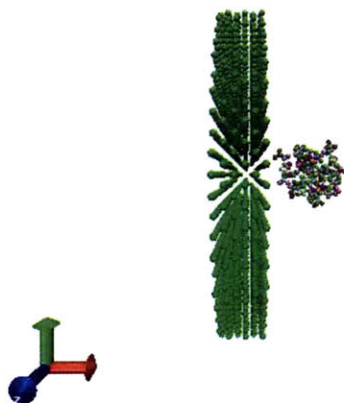
(a) Initial condition with 8 EMI-BF$_4$ molecules.
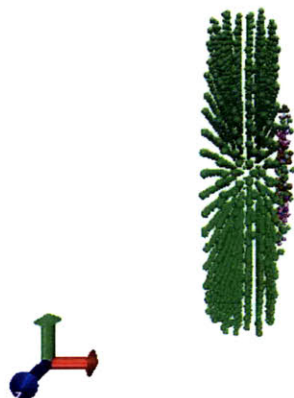
(b) Equilibrated condition with 8 EMI-BF$_4$ molecules.

Figure 9-4: Equilibration of 8 EMI-BF$_4$ molecules and tungsten plate.
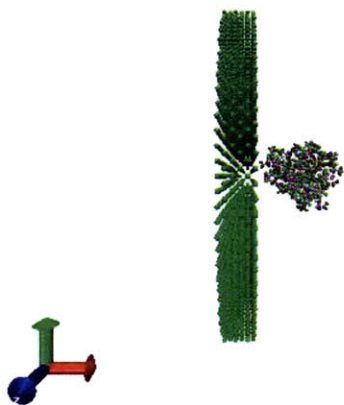
(a) Initial condition with 27 EMI-BF$_4$ molecules.
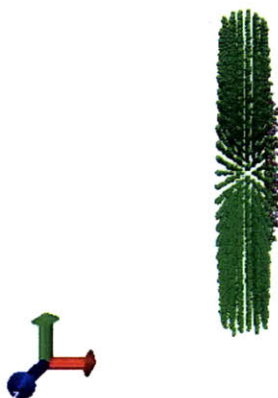
(b) Equilibrated condition with 27 EMI-BF$_4$ molecules.

Figure 9-5: Equilibration of 27 EMI-BF$_4$ molecules and tungsten plate.
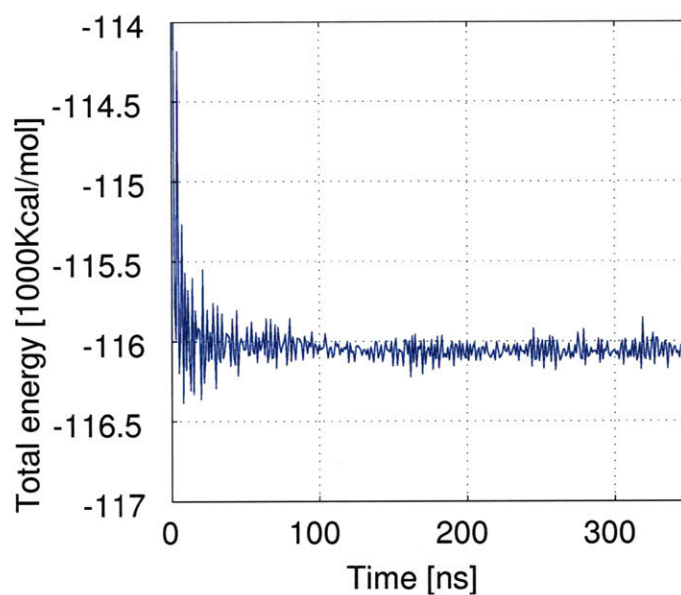
(a) 8 EMI-BF$_4$ molecules and tungsten plate.
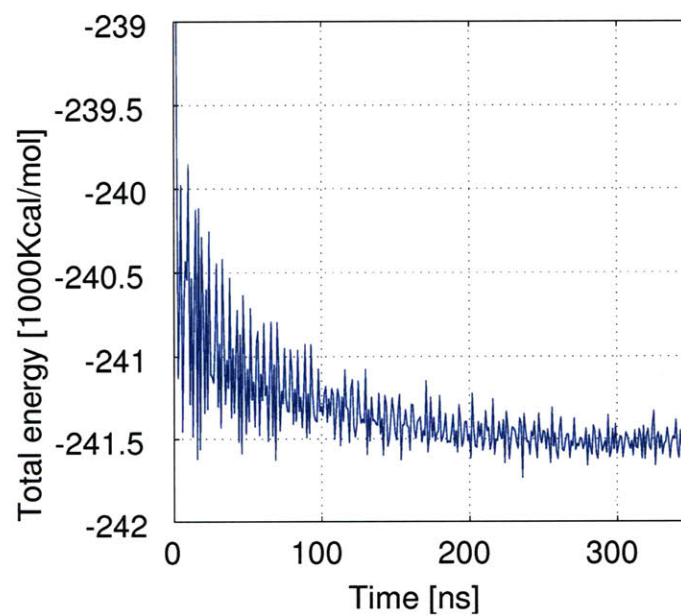
(b) 27 EMI-BF$_4$ molecules and tungsten plate.

Figure 9-6: (a) (b) Total energy profile of equilibration with EMI-BF$_4$ molecules and tungsten plate.
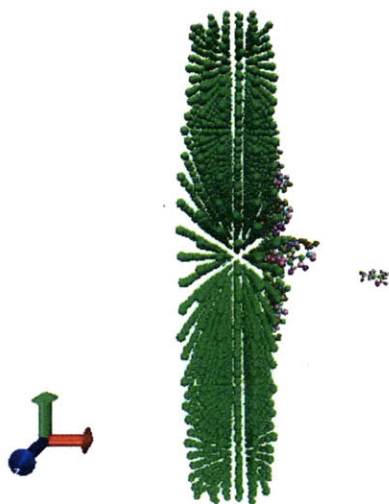
Figure 9-7: EMI$^+$ Ion emission from tungsten surface.

is observed through a surface charge distribution. However, in the system with a surface charge, it can be seen that a single molecule is emitted from the the edge of the tungsten surface where the electric field is strongest. This emission occurs at a surface charge distribution which corresponds to 6.0 V/nm. This reinforces the notion that a modified surface charge model is needed to model perpendicular ion emission The number of ions emitted is larger in the system with 27 molecules as shown in table 9.1. From the ion emission tendency, the LJ potential of tungsten atoms seems to work properly, though further investigation with more layers of EMI-BF$_4$ is needed to compare against experimental values. Also, there is the more interesting aspect of this type of simulations, namely, the ionic (electrochemical) interactions of counterions with metal structure. That might require some form of reactive MD.

Table 9.1: Ion emission profile for 27 EMI-BF$_4$ molecules and tungsten plate. (a) Ion emission under external E field with 8 EMI-BF$_4$ molecules, (b) Ion emission with surface charge with 8 EMI-BF$_4$ molecules, (c) Ion emission under external E field with 27 EMI-BF$_4$ molecules, (d) Ion emission with surface charge with 27 EMI-BF$_4$ molecules. Parenthesis indicates the time when the first ion emission is observed.

Electric field [V/nm]	(a)	(b)	(c)	(d)
3.0	-	-	-	-
3.5	◯ (138 ps)	-	◯ (139, 140 ps)	-
4.0	◯ (41, 182 ps)	-	◯ (19, 92, 113 ps)	-
5.0	◯ (1, 2, 7 ps)	-	◯ (3, 4, 16, 17 ps)	-
6.0	◯ (Every 1 ps)	◯ (198 ps)	◯ (Every 1 ps)	◯ (172 ps)

Chapter 10

Conclusions and Future Work

10.1 Summary of Results and Contributions

Atomistic modeling has the potential to be a versatile tool to reveal the physics of electrosprays. Preliminary studies for electrospray thrusters have been done by molecular dynamics simulations of ionic liquid droplets. The goal is to establish the first milestone of multi-scale modeling of electrosprays to reveal their mechanisms mainly based on the analysis of ion emission current and activation energy.

Current was measured by keeping track of the number of emitted ions from ionic liquid droplets under two conditions: fixed temperature (300 [K]) at various electric fields and fixed electric field (1.4 [V/nm]) at various temperatures (250 - 450 [K]). Electric current analysis was conducted using simulation results for the first time and the obtained total current density was reasonably well matched with experimental values. These results show ion emission of both solvated ions and non-solvated ions with a largest number of solvation of $n = 4$ in the positive side and $n = 5$ in the negative side. But $n = 0$ was by far more common. Activation energy analysis was made by fitting current vs. temperature curves with a Schottky-type model. This resulted in slightly lower values for the activation energy compared to experimental data with an average error of approximately 10 percent. The potential energy of droplets is also measured for various electric fields (1.2-2.0 [V/nm]) as an alternative to study activation energy under external electric fields. It is found that this method

is greatly affected by droplet deformation so only the first five or six emitted ion are used for the analysis. This analysis agrees relatively well with the latest experimental results for nano-droplets. Activation analysis through internal electric fields was also considered. The energy drop corresponded well to a rough analytical estimation. The summary of activation energy for each method is shown in table 10.1.

Table 10.1: Approach and activation energies.

Efield	Method	Activation energy per ion [eV]
External	Schottky fitting	1.4
	Droplet potential energy	1.8
Internal	NVT	0.2
	NVE	0.1

Propulsion properties have been investigated applying the ion emission results from droplets and electric field distributions along the liquid surface using the sphere-on-cone model. Thrust, Isp and current from one Taylor cone were calculated for both positive and negative polarities.

A final model was presented for the interaction between a liquid droplet and a solid have been observed using full AMBER force field model. Electric fields from a surface charge distribution was applied which gives a decaying field model that is closer to reality. The results indicate that the surface charge would work but the modification for the charge distribution and force field are needed for more realistic model.

Molecular dynamics simulations yield reasonable predictions for the activation energy of ionic liquids. Further research is necessary as mentioned in section 10.2, however, atomistic modeling is a promising way to understand this nano-scale phenomena.

10.2 Recommendations for Future Work

10.2.1 MD Simulation of Droplets

As indicated in chapter 6 and 7, there are several problems in the droplet simulations. Among them:

a. Moving droplet

Under external electric fields, the floating droplet moves along the electric field when it is charged due to ion emission. It is possible to analyze ion emission with the moving droplet but it prevents from a simple kinetic and potential energy analysis and may affect the energy calculations especially when a larger droplet is used with more ion emission because it also gives shorter time to accelerate the droplet itself.

The suggested solution is fixing four or five molecules placed at the center of the droplet. This is artificial but it should not affect too much the behavior of surface ions when a droplet is large enough and the atoms keep their partial charges and LJ potentials. The fixing should be made after the droplet is fully relaxed so that no more rotation occurs due to dipoles.

b. Number of molecules

The largest number of atoms in this work is 3000, but in general MD is able to handle more than ten to hundred billions of atoms. However, this is possible when special treatments, such as periodic boundary conditions or a reasonable neighbor list are applied and the code is run on "Teraflop" computers which require more than 1000 Opteron CPUs and large memory. (The estimation of computational time can be made with flops per clock per CPU for each computer.) One of the reasons for the limited number of molecules is the time step restriction (section 5.1.4) which requires approximately 1,000,000 iteration steps to cover only 1 [ns] trajectories. In addition to massive iterations, pair

potentials, especially long-range Coulomb potentials, increase computational burden due to the summations of every combination of particles thus scaling as N^2. Cutoff distances and neighbor lists can reduce this amount but this trade-offs with the accuracy of the potential calculation. Also, periodic boundary conditions are difficult to apply to droplet systems which are isolated from their surroundings. Thus, to tackle on larger systems, fast CPUs and large memories or appropriate modeling of systems are necessary. To observe an ion emission from liquid surfaces, it might be necessary to analyze a large plate of liquid instead of droplets, including periodic boundary conditions and apply external electric fields. If it is necessary to keep investigating droplet physics, NSF supercomputer is available for larger computations. [78]

c. Fraction of solvated ions

As shown in section 7.1, the fraction of solvated ions against non-solvated ions are small although experimental results show that monomer and dimer almost give same percent of total current in negative side and 4:6 in positive side. [52] This indicates that solvated ions in the simulation are easy to break, id est, there is a possibility that the coefficients of the force field are not appropriate in this case. The force field is validated in equilibrium states [51], however, apparently not under strong electric fields. In reality, the external electric fields might change the partial charge which atoms have and even the van der Walls potential. Another possibility is the effect of different electric field distributions: Taylor cone and constant electric fields, a condition that can be represented as a droplet placed between parallel plate electrodes. Further consideration is also required for the value of dielectric constant of the ionic liquid.

10.2.2 MD Simulation of Liquid and Solid

Further investigation is necessary mainly for the selection of an adequate force field. Currently it is impossible to mix up two different force fields in one MD simulation and the AMBER force field is the best option for organic materials but not for metals.

The reason that metals have different force fields can be described by their bonding system. Organic materials have pair potentials as inter molecular potentials, but on the other hand, metals have multi-body potentials in which bond strength is weaker at the surface of crystals. This is affected by quantum mechanical effects that describe the influence of the electron gas. Embedded atom method (EAM) potentials are used as force fields for metals, however, it does not have options to calculate liquids. It is known that the first-principle based ReaxFF has an ability to calculate two-phase systems although it is not capable get to calculate ionic liquids because lacks many atomic interaction types. We might be able to wait for ReaxFF to add new atoms but there is another option to create a force field called CVFF using appropriate software. [79] Technically it is possible to obtain the force field by direct calculation but this is not recommended because the process takes too much time in order to adjust the potential curve until obtaining the appropriate values of parameters for every intra- and inter- atomic potential. The software for CVFF force field is material "Material Studio" and the CVFF force field also works on LAMMPS. [80]

Electrochemical effect between solid and liquids would require a quantum method because molecular dynamics simulation does not directly calculate the motion of electrons. The problem of quantum methods is that they handle smaller number of atoms than MD. Thus it might be difficult to see mesoscopic phenomena such as Taylor cone with QM calculation due to the limited capacity and processing speed of machines.

10.2.3   Other Simulation Techniques

Other than molecular dynamics simulation, PIC (Particle in Cell) model is one of options to investigate behavior of ion jets. The detail is described in Appendix C.

Appendix A

Validation of MD simulation

A.1 Relaxation Time

The relaxation time of the EMI-BF$_4$ droplets under electric fields are checked. The droplets have 125 EMI-BF$_4$ molecules and these were all equilibrated at 300 [K] using thermostat [64] before the electric fields are applied. The time when first ion is emitted is assumed when the relaxation is completed and the time of five different samples in each electric field strength are averaged out. Figure A-1 shows the obtained result both for positive and negative emissions. We can see that the simulation values are in same order with typical relaxation time which is in order of 100-200 ps obtained from arguments in section 3.1.
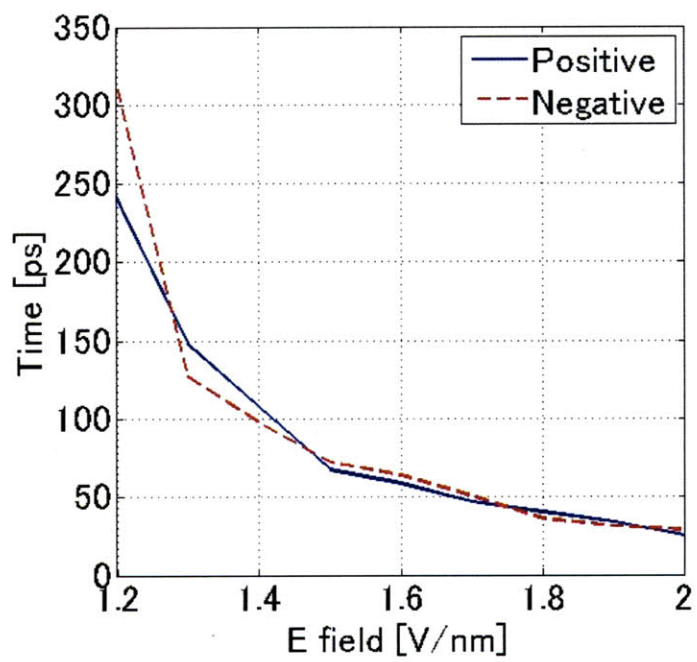
Figure A-1: Charge relaxation time

A.2 Evaporation Temperature

The evaporation temperature is investigated for EMI-BF$_4$ droplet with 64 molecules.

Starting from room temperature, temperature is increasing using Nose Hoover thermostat with dumping of 100 [K] as shown in figure A-2. Force fields of molecules are same as before [51], but there is no electric field in this case. The neutral ion emission was observed at approximately 1140K which is higher than experimental value (approximately 400 [K]). However, the experimental value is not obtained by a nano droplet neither emission of one molecule. Therefore further investigation is needed to explore the evaporation temperature of ionic liquids.
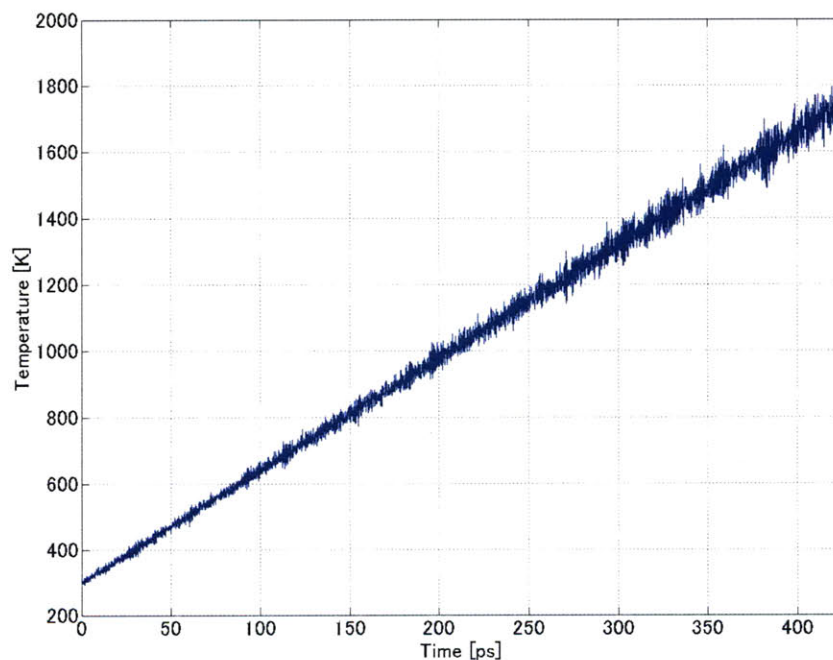
Figure A-2: Temperature transition

Appendix B

Computation

B.1 Molecular Dynamics Software

The LAMMPS (http://lammps.sandia.gov/) MD software has been used throughout this research. All the descriptions and explanations of commands for input files can find on the website. To make LAMMPS run on the SPL cluster machine, OpenMPI option is selected.

B.2 Visualization Software

B.2.1 General Information

Visual Molecular Dynamics (VMD) was used for visualization of MD simulation results. VMD is developed by theoretical and computational biophysics group in University of Illinois at Urbana-Champaign and is available for free from the link below.

http://www.ks.uiuc.edu/Research/vmd/

Instructions and tutorials can be also found on the website. As for visualization of LAMMPS results, we use dump and dcd files to load on the VMD.

B.2.2   Ion Tracking

An ion tracking script was created to make movies following moving droplets. This script was based on Dr. Axel Kohmeyer's work and the details can be found in section 6.2 of the link below.

http://sites.google.com/site/akohlmey/redirect/cpmd-vmd.pdf

The following is the script for our EMI-BF$_4$ droplet. Underlines show parts where we needed to make modifications depending on the files and target ions.

```
#——————————————————————————
# ion tracking code for EMI-BF4
#——————————————————————————

# load trajectory:
mol new {(dump file name)} type lammpstrj waitfor all
mol addfile {(dcd file name)} type dcd waitfor all
#mol delrep 0 top
#mol selection type 1 2 3 4 5 6 7 8 9 10

set molid 1
set hoffs 0

# let all selections be recalculated for each frame
# and smooth the trajectory a little bit for all representations
# that's part two of the magic.
set n [molinfo $molid get numreps]
for {set i 0} {$i < $n} {incr i} {
mol selupdate $i $molid on
```

```
mol smoothrep $molid $i 2
}


proc do_realign {args} {
global molid chist hcount hoffs dhist

♮ this is the axis to align to
♮set avec [vecnorm {1.0 0.0 0.0}]
♮ this is the sliding window size
set asize 5


♮ initialize the cache counters
if ([info exists hcount]) { } else {
set hcount 0
set hoffs -1
}


♮ find center
set sel [atomselect $molid "underlineindex (atom ID) or index (atom ID)"]
lassign [$sel get {x y z}] emi1 emi2
set cent [vecscale [vecadd emi1emi2] 0.5]
♮set dir [vecsub emi1emi2]


♮ store data in cache for sliding window averaring
if {$hcount < $asize} then { incr hcount }
incr hoffs
if {$hoffs >= $hcount} then { set hoffs 0 }
set chist($hoffs) $cent
♮set dhist($hoffs) $dir
```

```
♯ calculate averages
set csum [veczero]
♯set dsum [veczero]
for {set i 0} {$i < $hcount} {incr i} {
set csum [vecadd $csum $chist($i)]
♯set dsum [vecadd $dsum $dhist($i)]
}
set csum [vecscale [expr 1.0/[expr $hcount * 1.0]] $csum]
♯set dsum [vecnorm $dsum]

♯ get rotation axis
♯set rvec [vecnorm [veccross $dsum $avec]]

♯ set origin
molinfo $molid set
{center_matrix}
[list [trans origin $csum] ]
♯[trans axis $rvec [expr acos([vecdot $dsum $avec])] rad]]

♯ clean up selections
$sel delete
}

scale to 0.01
trace variable vmd_frame(1) w do_realign


♯ go back to the start of the trajectory.
♯animate style rock
♯animate goto start
```

B.3 SPL Cluster Machine and Execution of LAMMPS

All the simulation of this work has been done using SPL cluster machine (spl.mit.edu). It has 16 nodes with four AMD Opteron cores per node and two nodes with 8 Shanghai cores per node. OS is Red hat enterprise Linux and all the basic options for numerical simulations are available. However, it is necessary to modify bash file of an account to install the LAMMPS on the account before making LAMMPS. The ".bashrc" file at a home directory of an account needs to be:

♯ .bashrc

♯ Source global definitions

if [-f /etc/bashrc]; then

. /etc/bashrc

fi

♯ User specific aliases and functions

PATH=$PATH:/home/(user name)/bin

Modification of a make file is also required depending on the bash settings. The "Makefile.openmpi" needs to be modify. Here are the first half of the makefile in latest (Feb2010) version of LAMMPS. It is necessary to add "CCFLAG" and "LINKFLAG".

♯ openmpi = Fedora Core 6, mpic++, OpenMPI-1.1, FFTW2

SHELL = /bin/sh

♯ ————————————————————————————————

♯ compiler/linker settings

♯ specify flags and libraries needed for your compiler

CC = mpic++

CCFLAGS = -O2 -funroll-loops -DFFT_FFTW -DLAMMPS_GZIP

-fstrict-aliasing -Wall -W -Wno-uninitialized

-g -O -I/home/(username)/include -I/opt/openmpi.gcc/
include -I/opt/openmpi.gcc/include/openmpi

DEPFLAGS = -M

LINK = mpic++

LINKFLAGS = -g -O -L/home/(username)/lib -L/opt/
openmpi.gcc/lib -L/opt/openmpi.gcc/bin/

LIB = -lstdc++

ARCHIVE = ar

ARFLAGS = -rcsv

SIZE = size

♯ —————————————————————————————

This file is updated frequently and formats are slightly different in each version of LAMMPS, but the modifications are same.

The OpenMPI is used for parallelization to run LAMMPS and the command is executed in a shell script.

An example of the shell script is as following:

cd (folder name)

time mpirun (execution file) < (input file)

Here, the execution file for OpenMPI in LAMMPS is "lmp.openmpi". The shell script file needs to have an extension of ".sh" and it is run by "qsub" command assigning nodes to parallelize. The example of the command is:

$$qsub \quad -l \quad nodes \quad = \quad (node\ name) : ppn = (number\ of\ CPU)$$

$$+ \quad (node\ name) : ppn = (number\ of\ CPU) \quad (shell\ script\ file)$$

The details of other files (input file, data file etc...) can be found in the LAMMPS manual on the website (http://lammps.sandia.gov/).

Appendix C

PIC model

PIC simulation has been done to try to observe interactions between ion jets. The detail descriptions of PIC is explained in M.S. thesis by Fife [81].

C.1 Code Modification

The original code was developed by Prof. Paulo Lozano and modifications were applied to calculate ion emissions. The modified code was able to increase the number of sources and also can read RPA data obtained by an experiment. The RPA data provided an information about the fractions of solvated ions in ion jets. We use RPA data of an ionic liquid EMI-I (1-Ethyl-3-methylimidazolium Iodide) obtained by Tim Fedkiw, MIT (figure C-1).

C.2 Two Ion Jets

Figure C-2 shows visualization of the simulation results in chronological order. The simulation time step is 5 [ns] and currents for monomer and dimer are 63 [nA] and 97 [nA] respectively. The beams are both in negative polarity. Interaction can be seen from jet formations which are apparently not straight jets. It is necessary to verify the current model and further investigation are expected to adapt the model to array
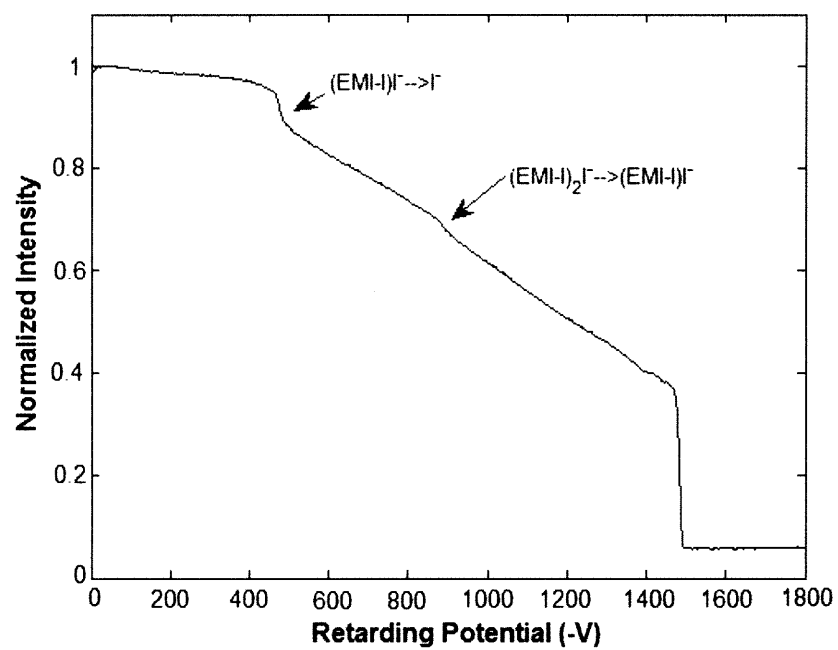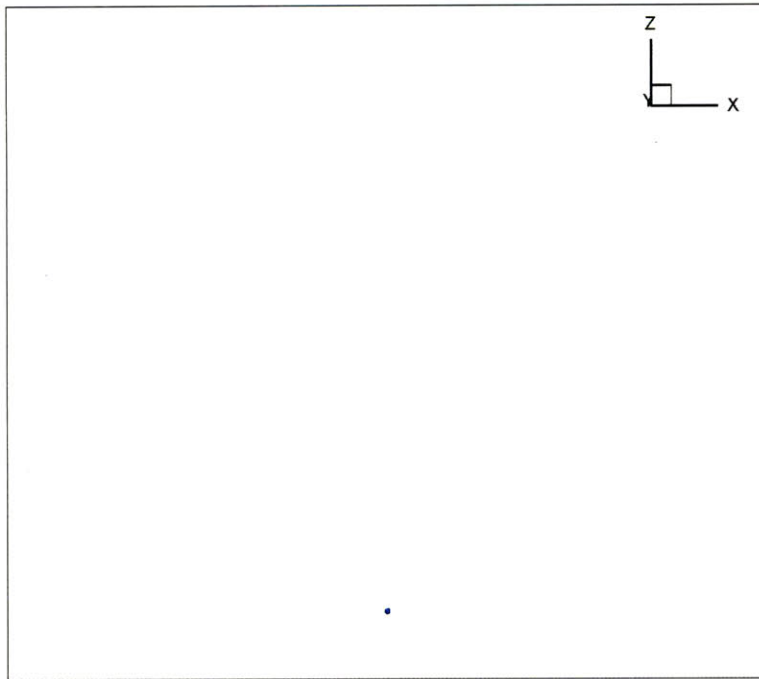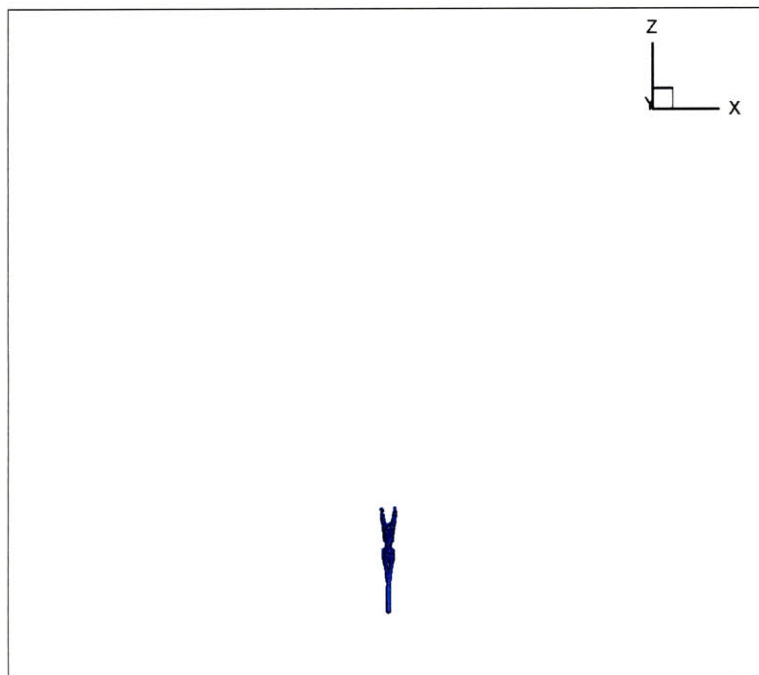
Figure C-1: RPA data for EMI-I. Courtesy of T. Fedkiw (MIT)

of electrosprays.

(a) 300K

(b) 350K
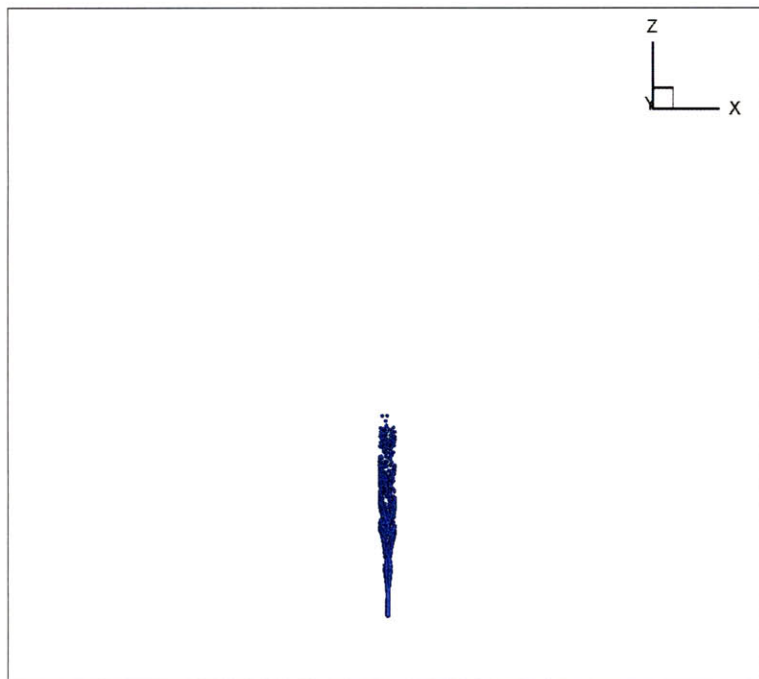
(c) 400K
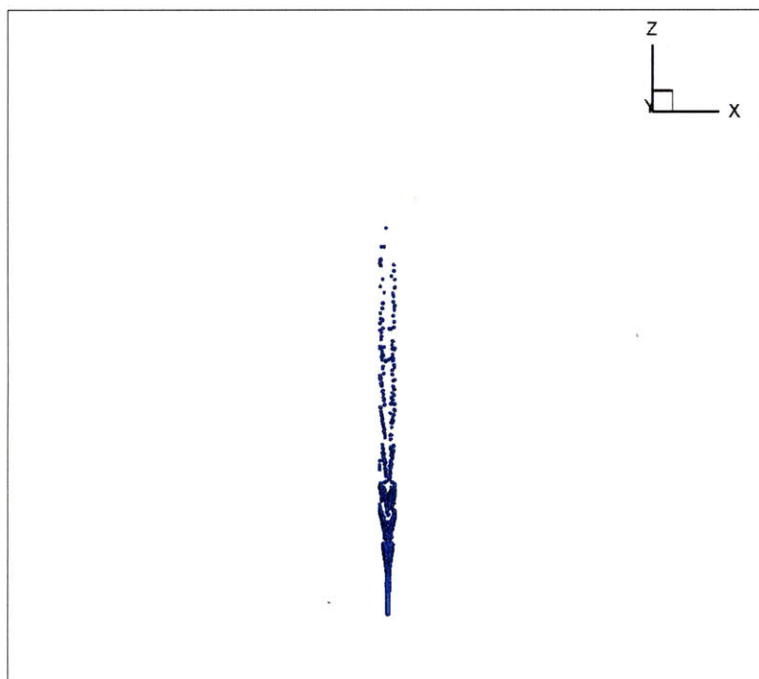
(d) 400K

Figure C-2: Equilibrium state of EMI-BF$_4$ (a) 300K (b) 350K (c) 400K

Bibliography

[1] Geoffery Taylor. Disintegration of water drops in an electric field. In *Proceedings of the Royal Society of London*, volume 280 of *A Mathematical and Physical Sciences*, pages 383–397. The Royal Society, 1964.

[2] John B. Fenn, Matthias Mann, Chin Kai Meng, Shek Fu Wong, and Craig M. Whitehouse. Electrospray ionization for mass spectrometry of large biomolecules. *Science*, New Series 246:64–71, 1989.

[3] A. Jaworek. Electrospray droplet sources for thin film deposition. *J. Mater Sci*, 42:266–297, 2007.

[4] D. Li and Y. N. Xia. Electrospinning of nanofibers: Reinventning the wheel? *Adv. Mater.*, 16:1151–1170, 2004.

[5] W. Deng, J.F. Klemic, X. Li, M.A, Reed, and A. Gomez. Liquid fuel micro-combustor using microfabricated multiplexed electrospray sources. *Proceedings of the Combustion Institute*, 31.

[6] W. Deng, J.F. Klemic, X. Li, M.A, Reed, and A. Gomez. Increase of electrospray throughput using multiplexed microfabricated sources for the scalable generation of monodisperse droplets. *J. Aerosol Sci.*, 37:696–714, 2006.

[7] A.G. Fedorov and F.L. Degertekin. Scanning mass spectrometry probe for biochemical imaging. *Electronics Letters*, 42(14), 2006.

[8] Jon Orloff, Mark Utlaut, and Lynwood Swanson. *High resolution focused ion beams: FIB and its applications.* Springer, New York, 2002.

[9] editor Jon Orloff. *Handbook of Charged Particle Optics.* CRC Press, Florida, 1997.

[10] A. Zorzos. The use of ionic liquid ion sources (ilis) in fib applications. *MIT M.S. Thesis*, May 2009.

[11] A. Nollet. Recherches sur les causes particulieres des phénomenes électrique; chez les frères guérin, 1749.

[12] G.Magnus. Hydraulische undersuchungen. *Ann. Phys. Chem.*, 106(1), 1859.

[13] L. Rayleigh. On the equilibrium of liquid conducting masses charged with electricity. *Philos. Mag.*, 14:184, 1882.

[14] J. Zeleny. The electrical discharge from liquids points, and a hydrostatic method of measuring the electric intensity at their surfaces. *Phys. Rev.*, 3(2):69–91, 1914.

[15] J. Zeleny. Instability of electrified liquid surfaces. *Phys. Rev.*, 10(1):1–8, 1917.

[16] V.E. Krohn Jr. *Liquid metal droplets for heavy particle propulsion*, volume 280. A. C. Press, N.Y. - London, 1961.

[17] V.E. Krohn Jr. Glycerol droplets for electrostatic propuslion. Berkeley, CA, 1962. ARS Electric propulsion conference.

[18] A. G. Baley. Investigation of a single spraying site of a colloid thruster. *J. Phys. D: Appl. Phys.*, 6(2):276–288, 1973.

[19] G.I. Taylor. Disintegration of water drops in an electric field. *Proceedings of the Royal Society of London*, 280:383–397, 1964.

[20] J.B. Fenn. Electrospray wings for molecular elephants (novel lecture). *Angew. Chem., Int. Ed.*, 42(33):3871–3894, 2003.

[21] L. Romero-Sanz, R. Bocanegra, M. Gamero-Casta no, and J. Fernandez de la Mora. Source of heavy molecular ions based on taylor cones of ionic liquids operating in the pure ion evaporation regime. *J. Appl. Phys.*, 94(5):3599–3601, 2003.

[22] P. Lozano and M. Martínez-Sánchez. Ionic liquid ion sources: characterization of externally wetted emitters. *J. Colloid Interface Sci.*, 282:415–421, 2005.

[23] Y. Chiu, B.L. Austin, R.A. Dressler, D. Levandier, P.T. Murray, P. Lozano, and M. Martínez-Sánchez. Mass spectrometric analysis of colloid thruster ion emission from selected propellants. *J. Prop. Power*, 21:416–423, 2005.

[24] J. V. Iribarne and B. A. Thomson. On the evaporation of small ions from charged droplets. *J. Chem. Phys.*, 64(6):2287–2294, 1976.

[25] B. A. Thomson and J. V. Irinarne. Field induced ion evaporation from liquid surfaces at atmospheric pressure. *J. Chem. Phys.*, 71:4451–4463, 1979.

[26] I. G. Loscertales and J. Fernández de la Mora. Experiments on the kinetics of field evaporation of small ions from droplets. *J. Chem. Phys.*, 103:5041–5060, 1995.

[27] R. G. Jahn. *Physics of Electric Propulsion*. McGraw Hill Book Co., 1968.

[28] K. Kuriki and Y. Arakawa. *Introduction to Electric Propulsion*. University of Tokyo Press, 2003.

[29] M. Martínez-Sánchez. Space propulsion lecture notes. *MIT*.

[30] R.S. Legge Jr., P.C. Lozano, and M. Martínez-Sánchez. Fabrication and characterization of porous metal emitters for electrospray thrusters. Florence, Italy, 2007. The 30th International Electric Propulsion Conference.

[31] D. G. Courtney and P. Lozano. Development of ionic liquid electrospray thrusters using porous emitter substrates. volume 2009-b-51, Tsukuba, Japan, 2009. The 27th International Symposium on Space Technology and Science.

[32] S. Marcuccio, A. Genovese, and M. Andrunucci. Experimental performance of field emission microhrusters. *J. Propul Power*, 14(5):774–780, 1998.

[33] P. Lozano. Studies on the ion-droplet mixed regime in colloid thrusters. *MIT Ph.D. Thesis*, Feb. 2003.

[34] P. McNamara, S. Vitate, and K. Danzmann. Lisa pathfinder. *Class. Quamtum Grav.*, 25(114034), 2008.

[35] M.N.W. Gronendijk, F. Tardaguila, and R.J. Koopmans. Initial development of a miniature cold gas propulsion system for nano/micro-satellites. May 2008.

[36] J. Fernández de la Mora and I.G. Loscertales. The current emitted by highly conducting taylor cones. *J. Fluid Mech.*, 260:155–184, 1994.

[37] P. Lozano. Personal communication. 2010.

[38] K. A. Dill and S. Bromberg. *Molecular Driving Forces - Statistical Thermodynamics in Chemistry and Biology*. Garland Science, New York U.S.A., London UK, 2002.

[39] Martyn J. Earle, José M.S.S. Esperanç, Manuela A. Gilea, José N. Canongia Lopes, Luís P.N. Rebelo, Joseph W. Magee, Kenneth R. Seddon, and Jason A. Widegren. The distillation and volatility of ionic liquids. *Nature*, 439:831–834, 2006.

[40] B. Gassend. A fully microfabricated two-dimensional electrospray array with application to space propulsion. *MIT Ph.D. Thesis*, May 2007.

[41] James P. Armstrong, Christopher Hurst, Robert G. Jones, Peter Licence, Kevin R. J. Lovelock, Christopher J. Satterley, and Ignacio J. Villar-Garcia. Vapourisation of ionic liquid. *Phys. Chem. Chem. Phys.*, (9):982–990, 2007.

[42] H. Ohno. *Electrochemical Aspects of Ionic Liquids*. John Wiley and Sons, Inc., New Jersey, 2005.

[43] A. Karkamkar, C. Aardahl, and T. Autrey. Recent developments on hydrogen release from ammonia borane. *Material Matters*, 2(2):6–9, 2007.

[44] P. Giridhar, K. A. Venkatesan, T. G. Srinivasan, and P. R. Vasudeva Rao. Electrochemical behavior of uranium(vi) in 1-butyl-3-methylimidazolium chloride and thermal characterization of uranium oxide deposit. *Electrochimica Acta*, 52(9):3006–3012, 2007.

[45] B. Wu, R. G. Reddy, and R. D. Rogers. Novel ionic liquid thermal storage for solar thermal electric power systems. *International Solar Energy Conference*, pages 445–451, 2001.

[46] M. Armand, F. Endres, D. R. MacFarlane, H. Ohno, and B. Scrosati. Ionic-liquid materials for the electrochemical challenges of the future. *Nature Materials*, 8:621–629, 2009.

[47] S. Hayashi and H. Hamaguchi. Discovery of a magnetic ionic liquid [bmim]fecl$_4$. *Chem. Lett.*, 33(12):1590–1591, 2004.

[48] J. Fuller, R. T. Carlin, and R. A. Osteryoung. The room temperature ionic liquid 1-ethyl-3-methylimidazolium tetrafluoroborate: Electrochemical couples and physical properties. *J. Electrochem. Soc.*, 144(11):3881–3886, 1997.

[49] A. B. McEwen, H. L. Ngo, K. LeCompte, and J. L. Goldman. Electrochemical properties of imidazolium salt electrolytes for electrochemical capacitor applications. *J. Electrochem. Soc.*, 146(5):1687–1695, 1999.

[50] J. Huang, P. Chen, I. Sun, and S.P. Wang. Nmr evidence of nydrogen bond in 1-ethyl-3-methylimidazolium tetrafluoroborate room temperature ionic liquid. *Inorganica Chimica Acta*, 320(1-2):7–11, 2001.

[51] Jones de Andrade, Elvis S. Boes, and Hubert Stassen. Computational study of room temperature molten salts composed by 1-alkyl-3-methylimidazolium cations - force-field proposal and validation. *J. Phys. Chem. B.*, 106(51):13344–13351, 2002.

[52] Robert S. Legge Jr. Fabrication and characterization of porous metal emitters for electrospray applications. *MIT M.S. Thesis*, June 2008.

[53] edited by R.R. Dogonadze et al. *The Chemical Physics of Solvation*. Elsevier, Amsterdam, New York, 1985.

[54] P. C. Lozano. Energy properties of an emi-im ionic liquid ion source. *J. Phys. D: Appl. Phys.*, 39:126–134, 2006.

[55] P. Lozano, M. Martínez-Sánchez, and J. M. Lopez-Urdiales. Electrospray emission from nonwetting flat dielectric surfaces. *J. Colloid Interface Sci.*, 276:392–399, 2004.

[56] A. Tolstogouzov, U. Bardi, O. Nishizawa, and M. Taniguchi. Mass spectrometric analysis of imidazolium-based ionic liquids by scanning atom probe. *Int. J. Mass Spectrom.*, 281:37–40, 2009.

[57] A. N. Zorzos and P. C. Lozano. Mass spectrometric analysis of imidazolium-based ionic liquids by scanning atom probe. *J. Vac. Sci. Technol. B.*, 26:2097–2102, 2008.

[58] A. M. Ga nán Calvo. Cone-jet analytical extension of taylor's electrostatic solution and the asymptotic universal scaling laws in electrospraying. *Phys. Rev. Lett.s*, 79:217–220, 1997.

[59] M. J. Buehler. *Atomistic Modeling of Materials Failure*. Springer, New York, 2008.

[60] J. E. Lennard-Jones. Cohesion. *The Proceedings of the Physical Society*, 43(240):461–482, 1931.

[61] James J. P. Stewart. Mopac: A semiempirical molecular orbital program. *J. Comput. Aided Mol. Des.*, 4(1):1–103, 1990.

[62] Sergey A. Katsyuba, Paul J. Dyson, Elena E. Vandyukova, Alla V. Chernova, and Ana Vidiš. Molecular structure, vibrational spectra, and hydrogen bonding of the ionic liquid 1-ethyl-3-methyl-1h-imidazolium tetrafluoroborate. *Helvetica Chimica Acta*, 87:2556–2565, 2004.

[63] Wendy D. Cornell, Pitor Cieplak, Christopher I. Bayly, Ian R. Gould, Jr. Kenneth M. Merz, David M. Ferguson, David C. Spellmeyer, Thomas Fox, James W. Caldwell, and Peter A. Kollman. Nanojets, electrospray and ion field evaporation: Molecular dynamics simulations and laboratory experiments. *J. Phys. Chem. A.*, 112:9628–9649, 2008.

[64] G. J. Martyna, M. E. Tuckerman, D. J. Tobias, and M. L. Klein. Explicit reversible integrators for extended systems dynamics. *Mol. Phys.*, 87(5):1117–1157, 1996.

[65] R. Hagiwara and Y. Ito. Room temperature ionic liquids of alkylimidazolium cations and fluoroanions. *J. Fluor. Chem.*, 105:221–227, 2000.

[66] A. A. Fannin Jr., D. A. Floreami, L. A. King, J. S. Landers, B. J. Piersma, D. J. Stech, R. L. Vaughn, J. S. Wilkes, and J. L. Williams. Properties of 1,3-dialkylimidazolium chloride-aluminum chloride ionic liquids. 2. phase transitions, densities, electrical conductivities, and viscosities. *J. Phys. Chem.*, 88:2614–2621, 1984.

[67] C. J. Hogan and J. Fernández de la Mora. Tandem ion mobility-mass spectrometry (ims-ms) study of ion evaporation from ionic liquid-acetonitrile nanodrops. *Phys. Chem. Chem. Phys.*, 11:8079–8090, 2009.

[68] N. Takahashi, M. Lieu, and P. Lozano. Atomistic numerical approach to electrospray thrusters. volume 2009-b-52, Tsukuba, Japan, 2009. The 27th International Symposium on Space Technology and Science.

[69] J. W. Ward and R. L. Selinger. Trajectory calculations of the extraction region of liquid-metal ion source. *J. Voc. Sci. Technol.*, 19:1082–1086, 1981.

[70] P. Lozano, B. Glass, and M. Martínez-Sánchez. Performance characteristics of a linear ionic liquid electrospray thruster. volume IEPC-2005-192, Princeton University, 2005.

[71] J. E. Stone, J. Gullingsrud, and K. Schulten. A system for interactive molecular dynamics simulation. pages 191–104, New York, 2001. 2001 ACM Symposium on Interactive 3D Graphics.

[72] W. Humphrey, A. Dalke, and K. Schulten. Vmd: Visual molecular dynamics. *J. Mol. Graph.*, 14(33), 1996.

[73] K. Tanaka, T. Kato, and Y. Matsumoto. Molecular dynamics simulation of vibration friction force due to molecular deformation in confined lubricant film. *J. Tribol*, 125:587–591, 2003.

[74] W. D. Luedtke, U. Landman, Y.-H. Chiu, D. J. Levandier, R. A. Dressler, S. Sok, and M. S. Gordon. Nanojets, electrospray and ion field evaporation: Molecular dynamics simulations and laboratory experiments. *J. Phys. Chem. A.*, 112:9628–9649, 2008.

[75] J. W. Daily. Molecular dynamics simulation of ion emission from nanodroplets of ionic liquids. *J. Propul. Power*, 24(5):981–986, 2008.

[76] N. Takahashi and P. Lozano. Computational investigation of molecular ion evaporation in electrospray thruster. volume AIAA-2008-4533, Hartford, 2008.

[77] M. Tuckerman, B. J. Berne, and G. J. Martyna. Reversible multiple time scale molecular dynamics. *J. Chem. Phys.*, 97:1990–2001, 1992.

[78] https://www.teragrid.org/.

[79] M. Buehler. Personal communication. 2009.

[80] http://lammps.sandia.gov/.

[81] J. M. Fife. Two-dimensional hybrid particle-in-cell modeling of hall thrusters. *MIT M.S. Thesis*, May 1995.